JGR Oceans

RESEARCH ARTICLE
10.1029/2025JC023103

Basal Melting Variability of the Ross Ice Shelf From Mixing Ratios of Simulated Water Masses (1993–2018) and Potential Climatic Drivers

Enrico Pochini[1,2,3], Andrea Bergamasco[4], Florence Colleoni[1], Manuel Bensi[1], Giorgio Budillon[5], Pasquale Castagno[6], Michael S. Dinniman[7], Pierpaolo Falco[8], Emanuele Forte[2], Vedrana Kovačević[1], and Stefanie L. Mack[9]

[1]National Institute of Oceanography and Applied Geophysics (OGS), Trieste, Italy, [2]University of Trieste, (UniTS), Trieste, Italy, [3]Now at Department of Earth and Atmospheric Sciences, University of Alberta, Edmonton, AB, Canada, [4]National Research Council - Institute of Polar Sciences, (CNR-ISP), Venice, Italy, [5]University of Naples Parthenope, (UniParthenope), Naples, Italy, [6]University of Messina, Messina, Italy, [7]Center for Coastal Physical Oceanography, Old Dominion University (CCPO-ODU), Norfolk, VA, USA, [8]Marche Polytechnic University, (UNIVPM), Ancona, Italy, [9]University of Tokyo, Tokyo, Japan

Key Points:

- A mixing ratios analysis applied to the water masses under the Ross Ice Shelf highlights their connection to basal melting over 1993–2018
- Simulated basal melting is 90 Gt/yr caused by: High Salinity Shelf Water 68%, modified Circumpolar Deep Water 25%, Antarctic Surface Water 7%
- Basal melting shows seasonal, interannual, and decadal variability. Decadal variations are potentially driven by Pacific teleconnections

Supporting Information:

Supporting Information may be found in the online version of this article.

Correspondence to:

E. Pochini and F. Colleoni,
pochini@ualberta.ca;
fcolleoni@ogs.it

Citation:

Pochini, E., Bergamasco, A., Colleoni, F., Bensi, M., Budillon, G., Castagno, P., et al. (2026). Basal melting variability of the Ross Ice Shelf from mixing ratios of simulated water masses (1993–2018) and potential climatic drivers. *Journal of Geophysical Research: Oceans*, *131*, e2025JC023103. https://doi.org/10.1029/2025JC023103

Received 3 JUL 2025
Accepted 19 JAN 2026

Author Contributions:

Conceptualization: Enrico Pochini, Andrea Bergamasco, Florence Colleoni
Data curation: Enrico Pochini
Formal analysis: Enrico Pochini
Funding acquisition: Florence Colleoni, Emanuele Forte
Investigation: Enrico Pochini
Methodology: Enrico Pochini, Andrea Bergamasco, Florence Colleoni
Project administration: Florence Colleoni

Abstract Several water masses circulate under the Ross Ice Shelf (RIS), the largest ice shelf in Antarctica, each causing basal melting with a specific spatio-temporal pattern. To investigate these patterns and their variability, we applied a mixing ratio analysis to simulated water masses from a new numerical ocean model of the Ross Sea. The simulation, which was run over 26 years (1993–2018) and which includes the RIS cavity, shows good agreement with seaborne and mooring observations. The total RIS basal melt rate is 90 Gt/yr on average, and is caused mostly by High Salinity Shelf Water (HSSW) (68%), which enters the western portion of the RIS cavity. In the eastern RIS, relatively warm modified Circumpolar Deep Water (mCDW) intrudes below a small portion of the RIS front, causing 25% of the total melting. Mainly near the Ross Island region, Antarctic Surface Water (AASW) is advected under the RIS, causing a small percentage (7%) of melting. A strong seasonal cycle is present in basal melting for all water masses. Melting by HSSW is stronger in winter, when salinification due to sea ice production is larger. By contrast, in the summer, reduced density gradients along the RIS front allow stronger intrusions of mCDW and AASW. Interannual variability is large for mCDW and AASW. Melting caused by HSSW shows decadal variability, mostly related to the salinity of HSSW, which is impacted by sea ice import from the Amundsen Sea and sea ice production in local polynyas, both potentially affected by Pacific teleconnections.

Plain Language Summary The Ross Ice Shelf melts at its base due to the influence of several water masses. The Ross Ice Shelf is, however, mostly shielded by cold, salty water and, therefore, has shown a weak response to ongoing climate change, in contrast with other seas and ice shelves around Antarctica. To better understand how different water masses affect its melting and how the water masses are influenced by climatic drivers, we examined the variability of basal melt over a 26-year period using a numerical regional ocean model. Our results show that cold and salty shelf water accounts for 68% of the total basal melt. Relatively warm water intruding from the open ocean (i.e., the oceanic heat source in the Southern Ocean) contributes 25%; finally, the surface layer, which is heated up during summer and advected under the Ross Ice Shelf, contributes 7%. Basal melt exhibits variations between seasons, and from year to year, but also decadal variations related to salinity change, which regulate the presence of the cold, salty water under the ice shelf. These changes are potentially related to atmospheric and oceanic processes in the tropical Pacific, which manifest in the Ross Sea and Ross Ice Shelf predominantly at decadal time scales.

1. Introduction

Satellite observations indicate that most Antarctic ice shelves have thinned over the past decades (e.g., Paolo et al., 2015; Rignot et al., 2013) primarily due to increased basal melting driven by relatively warm water masses from the Southern Ocean (Depoorter et al., 2013; Liu et al., 2015; Pritchard et al., 2012; Rignot et al., 2019). In contrast to "warm" sub-ice shelf cavities, which are sensitive to increased access of warm Circumpolar Deep Water (CDW) on the continental shelf, "cold" sub-ice shelf cavities—such as the Ross Ice Shelf (RIS) and the Filchner-Ronne Ice Shelf —are shielded by cold and salty Dense Shelf Waters (DSW). These "cold" cavities have

Resources: Andrea Bergamasco, Florence Colleoni, Pasquale Castagno, Michael S. Dinniman
Software: Enrico Pochini
Supervision: Florence Colleoni, Emanuele Forte
Validation: Enrico Pochini
Visualization: Enrico Pochini
Writing – original draft: Enrico Pochini
Writing – review & editing: Enrico Pochini, Andrea Bergamasco, Florence Colleoni, Manuel Bensi, Giorgio Budillon, Pasquale Castagno, Michael S. Dinniman, Pierpaolo Falco, Emanuele Forte, Vedrana Kovačević, Stefanie L. Mack

not exhibited any long-term acceleration in ice discharge in response to climate change (Paolo et al., 2015; Rignot et al., 2013; Smith et al., 2020). Instead, they show decadal variablity in surface elevation and mass balance (Adusumilli et al., 2020; Paolo et al., 2015).

This raises the question about the stability of the RIS and other cold-cavity ice shelves under changing climatic conditions. A warmer and fresher Southern Ocean could potentially alter the dynamics of the Antarctic Slope Front (ASF, Thompson et al., 2018). The ASF separates open-ocean water masses from those on the continental shelf. Where the prevailing winds are easterlies, the ASF is weak, allowing stronger intrusions of CDW onto the continental shelf. Where strong katabatic winds drive DSW formation, the dense water masses on the continental shelf cause the ASF to be a strong barrier to CDW intrusions, which may only occur by processes such as eddies (A. L. Stewart & Thompson, 2015), topography-stirred intrusions (Dinniman et al., 2011; Klinck & Dinniman, 2010; C. Wang et al., 2024), exchanges during DSW outflows (Morrison et al., 2020), and tides (Padman et al., 2009; Q. Wang et al., 2013). The ASF is currently in a "cold" or "dense" state in the Ross Sea, but changing climatic conditions can trigger a transition toward a "warm" regime through modification of continental shelf-break dynamics leading to increased intrusions of warm CDWthat may eventually reach the RIS cavity. Projected climate changes indicate potential regime shifts toward "fresher" and "warmer" conditions in some portions of the Weddell Sea and the Filchner-Ronne Ice Shelf (Hellmer et al., 2012; Naughten et al., 2021) and in the eastern Ross Sea, under the SSP5-8.5 scenario (Mathiot & Jourdain, 2023; Siahaan et al., 2022) by 2100. These density variations in water masses on "fresh" continental shelves (Thompson et al., 2018) may be induced by reduced salinity and warmer ocean temperatures, potentially involving a drastic reorganization of continental shelf circulation. This would allow enhanced intrusions of CDW into previously "cold" sub–ice-shelf cavities, although some studies indicate that changes in atmospheric circulation alone may be sufficient to cause such regime shift on some continental shelves (Spence et al., 2014). This highlights that the stability of ice shelves is subject to changing regional oceanographic properties.

Observations confirm that the Southern Ocean has been warming: a trend of 0.0042°C/yr has been observed since the 1950s in the intermediate-depth waters of the Southern Ocean (700–1,100 m) (Gille, 2002). Warming has also been detected in the bottom water layer of the continental shelf in several sectors of Antarctica (Schmidtko et al., 2014). This warming trend has been paralleled by multidecadal freshening of shelf waters observed in the Ross Sea between the 1950s and 2014 (Jacobs et al., 2002, 2022). In 2014, the trend reversed, indicating a salinification of the Ross Sea shelf waters (Castagno et al., 2019). This shift has been attributed to a combination of regional and remote climatic drivers (Silvano et al., 2020).

In general, several drivers can contribute to the observed salinity variability. Regional (Antarctic) drivers, include katabatic winds, changes in the strength of the westerlies (Southern Annular Mode), pressure fluctuations in the Amundsen Sea Low (Falco, Aulicino, et al., 2024; Xie et al., 2024), freshwater input and sea ice transported along the Antarctic coasts to the Ross Sea (Nakayama et al., 2014). External drivers, linked to tropical teleconnections (Li et al., 2021), propagate in the lower atmosphere and modulate the near-surface wind in the Pacific Sector of the Southern Ocean at interannual to decadal time scales (Holland & Kwok, 2012; Meehl et al., 2019; Zhang et al., 2024). These external drivers thus modulate sea ice transport (Jones et al., 2016), sea ice production (Silvano et al., 2016), air-sea heat fluxes, and sea-surface temperature (Haumann et al., 2016; Yuan, 2004). For further description of teleconnections impact on the Ross Sea, see Text S1 in Supporting Information S1. Natural and anthropogenically forced variability are, however, intertwined, which makes it difficult to disentangle the effect of one or the other on observed salinity changes (Jenkins et al., 2016). See Text S1 in Supporting Information S1 for a more detailed summary of the climatic indices and on the impact of teleconnections on the Ross Sea.

1.1. Ross Sea Water Masses

In the Ross Sea (Figure 1a), several water masses have been identified (Budillon et al., 2002; Falco, Aulicino, et al., 2024; Jacobs et al., 1979, 1985; Jacobs & Giulivi, 1999; Orsi et al., 1999; Russo et al., 2011). Shelf waters (SW) are found on the continental shelf at intermediate depths, and are colder than CDW (Figure 1b). In the western Ross Sea, a particularly high salinity form of SW, the High Salinity Shelf Water (HSSW), is produced by brine rejection during sea ice formation in coastal polynyas. HSSW fills most of the bottom of the Ross Sea in this sector and is a type of Dense Shelf Water (DSW). HSSW flows both toward the continental shelf break and the RIS cavity (Figure 1a). Under the RIS, because of the freezing point decrease with pressure/depth, HSSW

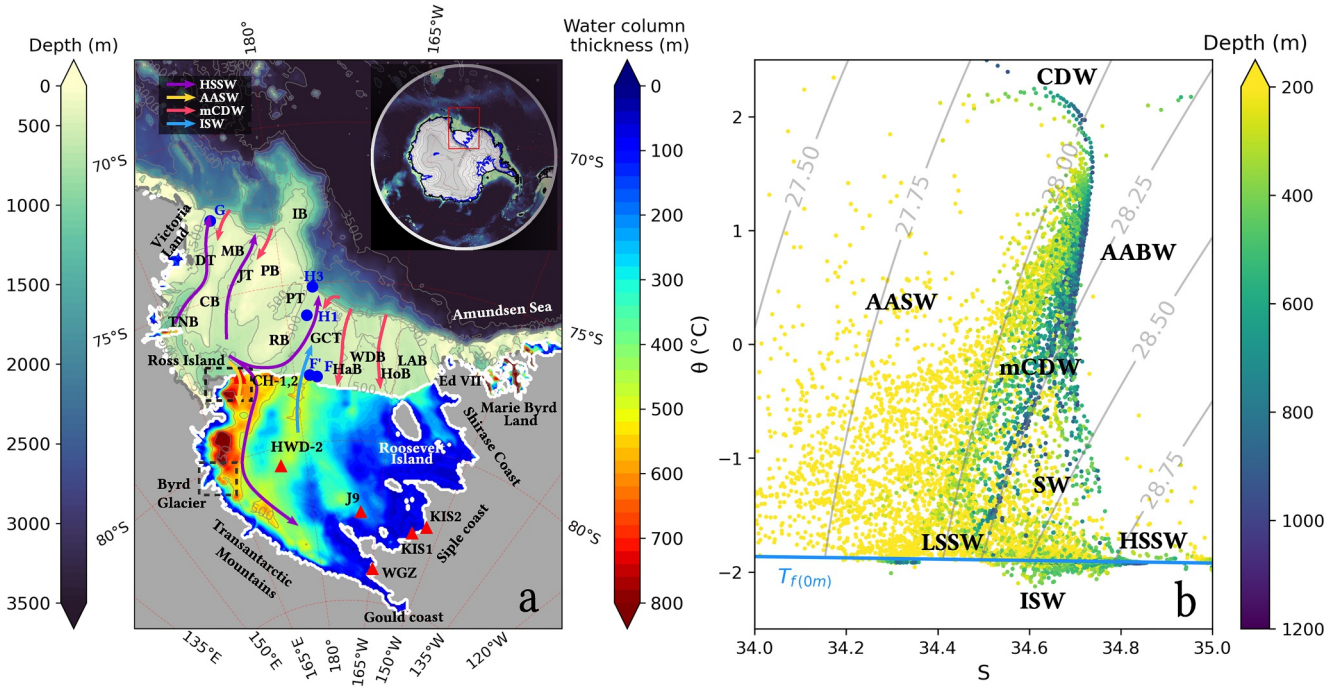

Figure 1. (a) Bathymetry employed in this Ross Sea configuration, Bedmap2 (updated to RTopo-2, Fretwell et al., 2013; Schaffer et al., 2014); water column thickness is shown below the ice shelves. The thick white line indicates ice shelf margins, including the grounding line. The gray region indicates topography above sea level or grounded ice sheet. The colored arrows identify the major water masses in the Ross Sea (acronyms explained in b), and their circulation pathways. Blue dots indicate the 5 locations of the moorings of the MorSea project used in this study. The red triangles indicate the sites where borehole measurements exist. (b) θ, S diagram of Conductivity-Temperature-Depth (CTD) data from the CLIMA (1996–2007) and AnSlopeIII (2004) campaigns in the Ross Sea, in the depth range 0–1,200 m. In situ temperature was converted to potential temperature in the ITS-90 definition with the Gibbs SeaWater (GSW) package. Salinity is expressed in practical units (PSU), according to the definition PSS-78. All measurements were resampled on levels evenly spaced at 50 m. The light blue line is the surface freezing point, T_f. The main water masses are labeled: Antarctic Bottom Water (AABW), Antarctic Surface Water (AASW), Circumpolar Deep Water (CDW), modified CDW (mCDW), Low/High Salinity Shelf Water (LSSW/HSSW), Ice Shelf Water (ISW), Shelf Waters (SW). Isopycnals of neutral density anomaly are added as gray contours, calculated with the Python interface to PreTEOS-10 neutral density Fortran code (https://github.com/guidov/pygamman_f2py). The major locations mentioned in this study are labeled in (a): CB = Crary Bank, DT = Drygalski Trough, Ed VII = King Edward VII peninsula, GCT = Glomar Challenger Trough, HaB = Hayes Bank, HoB = Houtz Bank, IB = Iselin Bank, JT = Joides Trough, LAB = Little America Basin, MB = Mawson Bank, PB = Pennel Bank, PT = Pennel Trough, RB = Ross Bank, TNB = Terra Nova Bay, WDB = Whales Deep Basin.

temperatures are usually above the in situ freezing point and can melt the ice-shelf base. HSSW is associated with "Mode 1" melting (Jacobs et al., 1992), the dominant mode of ice shelf basal melting in cold cavities.

In the eastern Ross Sea, by contrast, mixing with meltwater transported from the Amundsen-Bellingshausen Seas freshens the SW; this, together with weak sea ice production, leads to the formation of Low Salinity Shelf Water (LSSW) (Figures 1a and 1b). Along the continental slope, at depths between 300 and 1,000 m, we find CDW, which has relatively high temperature (up to 1°C) and intermediate density (Figure 1b). As it intrudes along the troughs over the continental shelf edge (Figure 1a), it mixes with the SW, losing heat; it is then termed "modified" CDW (mCDW) (Castagno et al., 2017; Jacobs & Giulivi, 1999; Russo et al., 2011). mCDW produces basal melting at intermediate depth (~300 m) along the eastern RIS front (Figure 1a). Melting by mCDW is referred to as "Mode 2" (Jacobs et al., 1992).

Antarctic Surface Water (AASW) is a low-salinity water mass that occupies the surface layer (100–200 m, Figure 1b). During summer, when sea ice opens, AASW is heated by solar radiation to temperatures a few degrees above 0°C. Observations indicate that this surface heat can access the ice-shelf cavity, primarily along the eastern flank of Ross Island (C. L. Stewart et al., 2019), where the RIS draft is very shallow, up to 70 m below sea level (Figure 1a). However, the mechanisms governing this process remain poorly understood (Jendersie et al., 2018; Malyarenko et al., 2019; C. L. Stewart et al., 2019). The associated basal melting occurs close to the ice-shelf front and is termed "Mode 3" (Jacobs et al., 1992).

Signals of AASW below the RIS were detected by Argo floats and seal-borne measurements in other regions along the RIS front (Falco, Krauzig, et al., 2024; Malyarenko et al., 2019). These smaller intrusions are thought to be caused by the accumulation of AASW and meltwater in a wedge-shaped layer (Malyarenko et al., 2019) which, if deep enough to reach the ice shelf base, enables the advection of AASW under the RIS by other mechanisms. Because of the large depth of the RIS front elsewhere other than near Ross Island, the wedge, there, may barely reach the depth of the RIS, and AASW intrusions are therefore much weaker and less extended. As water masses inside the RIS cavity exchange heat and salinity by melting the ice shelf base, they cool down and freshen. If they cool below the surface freezing point (~ -1.85°C), they become *supercooled*, and are termed Ice Shelf Water (ISW, Figure 1b), (Jacobs et al., 1970, 1985; Nelson et al., 2017). ISW outflows from the RIS cavity as plumes, near the 180° East location (Bergamasco et al., 2004; Jacobs et al., 1985; Jendersie et al., 2018; Smethie & Jacobs, 2005) at about 200–500 m depth and out of McMurdo Sound, on the western side of Ross Island (Robinson et al., 2014).

Each of these water masses, except the ISW, is affected by different atmospheric processes and interacts with the RIS on a wide range of spatio-temporal scales (e.g., Tinto et al., 2019). Despite ocean forcing being a first-order driver of ice shelf thinning, ice-ocean interactions are still poorly understood and represented in state-of-the-art stand-alone ice-sheet–ice-shelf models. Such models rely on parameterizations that do not fully capture the phenomenology of ocean processes in the sub-ice shelves cavities (e.g., Favier et al., 2019; Holland et al., 2008; Jourdain et al., 2020; Martin et al., 2011; Pollard & DeConto, 2012).

Observation-based estimates of pan-Antarctic basal melting rates have been achieved using indirect multi-method techniques, from satellite altimetry and InSAR, to simulated accumulation (Adusumilli et al., 2020; Das et al., 2020; Moholdt et al., 2014; Rignot et al., 2013) and calving flux (Depoorter et al., 2013). However, very few direct observations of the sub-ice shelf environments exist (Gwyther et al., 2020; McPhail et al., 2009, 2019; Nicholls et al., 2006; Schmidt et al., 2023; Wåhlin et al., 2024), and logistic and technological limitations only allow the exploration of small cavities. In the Ross Sea, Falco, Krauzig et al. (2024) provided the first year-round observations with Argo floats along the RIS and in a limited portion below the RIS frontal region. The RIS cavity, however, is not routinely accessed with Argo floats. Therefore, ice-ocean interactions are generally studied by means of ocean models, either coupled or uncoupled to the ice shelves, evaluated by comparison with available observations (Arzeno et al., 2014; Dinniman et al., 2003, 2015; Jendersie et al., 2018; Mack et al., 2019; Nakayama et al., 2019; Naughten et al., 2018; Richter et al., 2020). Melting modes are usually discriminated by a simple depth criterion for multi-mode cavities (Adusumilli et al., 2020; Jacobs et al., 1992), and no spatio-temporal relationship between water masses and basal melt has been established so far.

In the present study, we developed a new method to partition basal melting of the RIS into the different water masses in the Ross Sea, simulated with a 5-km regional model. The method, which is based on the Optimum MultiParameter analysis of the simulated water masses' temperature and salinity (Budillon et al., 2003; Tomczak, 1981), allows us to quantify the impact of each water mass on RIS basal melting and investigate their spatio-temporal variability over seasonal, interannual, and decadal timescales. The model, which resolves the RIS cavity, was run transiently over 1993–2018.

This paper is structured as follows. Section 2 details the numerical model configuration, the mixing analysis method, and its application to simulated basal melting. Section 3 is dedicated to model validation against available observations. Section 4 describes the simulated mixing ratios and the analysis of simulated basal melt in terms of spatio-temporal variability. Section 5 discusses the results, given their broader implications related to both teleconnections and methodological limitations. Section 6 draws some conclusions.

2. Methods

2.1. Regional Ocean Model Implementation

We implemented the Massachusetts Institute of Technology general circulation model (MITgcm, Marshall, Adcroft et al., 1997; Marshall, Hill, et al., 1997) on a regional configuration for the Ross Sea at 5-km horizontal resolution. The model grid is Cartesian and uniform in the horizontal direction but has variable Z-levels, with a thickness of 10–50 m over the continental shelf. The model allows circulation inside the sub-ice shelf cavities and thermodynamic interaction with ice shelves (Losch, 2008) via the three-equation formulation (Hellmer & Olbers, 1989; Jenkins et al., 2001). A dynamic sea ice module is included, but tidal forcing was not implemented. See Text S2 in Supporting Information S1 for more details on the regional setup.

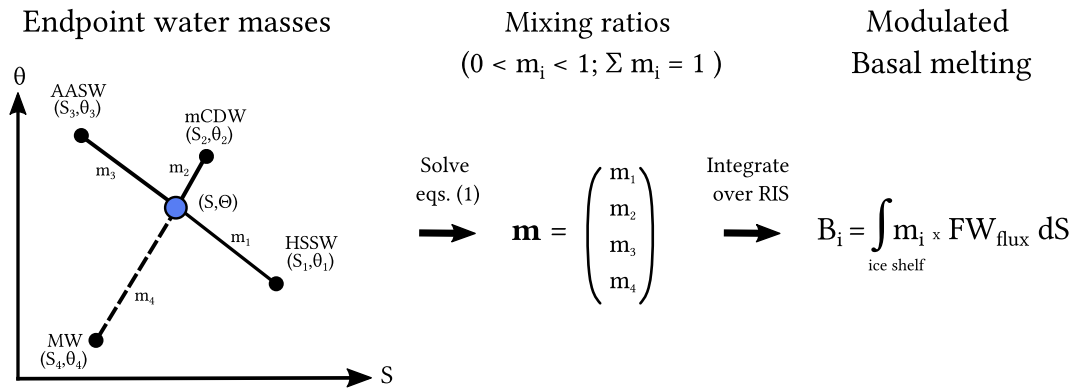

Figure 2. Schematic explanation of the mixing method applied to basal melting. The blue dot represents a water mass sample with properties (θ, S) in a grid point in contact with the ice shelf base. The four endpoints (High Salinity Shelf Water, Antarctic Surface Water, modified Circumpolar Deep Water, Meltwater) are represented by the black dots. The (θ, S) appear at the right-hand side of Equations 1 and 2 as a linear combination of (θ_1, S_1) to (θ_4, S_4) endpoints, with coefficients m_1 to m_4, which are functions of the distance between the sample and the endpoints in the (θ, S) space.

We run a transient simulation over 1993–2018 branched on a 6-year spin-up. The spin-up was run using a perpetual 1993-year forcing. Both spin-up and transient simulations were forced using the atmospheric reanalysis ERA5 (Hersbach et al., 2020) and the oceanic reanalysis GLORYS12V1 (Lellouche et al., 2021) (see Text S3 in Supporting Information S1 for more details on the boundary and initial conditions). The forcing fields were updated at a 3-hourly frequency for the atmosphere and at a monthly frequency for the ocean lateral boundaries. The length of the spin-up was chosen based on the early model work by MacAyeal (1984a) and radioactive geochemical tracer measurements at site J9 (Figure 1a) by Michel et al. (1979), who found that the ventilation time for the RIS cavity circulation was around 5–6 years; 6 years is also the spin-up time used in another Ross Sea model based on ROMS (Dinniman et al., 2007). More information about the numerical setup is provided in Text S2 and S3 in Supporting Information S1.

2.2. Water Masses Mixing Analysis

Each water mass in contact with the RIS base is decomposed as a mixing of endpoint water masses, characterized by their potential temperature and salinity $(\theta, S$, Figure 2). These endpoints are defined so as to represent the climatological characteristic (θ, S) of the non-mixed water masses as they enter the RIS cavity. To define them, we inspected a climatological distribution of the simulated water masses at the level of the RIS draft, in the (θ, S) space: the endpoints appear as the extreme points toward which the water masses' (θ, S) tend to fall (see Figure 6). We identified four endpoints, corresponding to the main Ross Sea water masses: HSSW, mCDW, AASW, and subglacial Meltwater (MW), which represent the effect of the melting ice shelf (see Section 2.2.1). As the "pure" water masses circulate in the RIS cavity they mix and they exchange heat and MW with the RIS; therefore, their (θ, S) properties become less pronounced. Notice that LSSW is not included in the list; LSSW is treated, in this study, as a mix of HSSW, mCDW, and MW.

The four endpoints have the following (θ, S) properties in units [PSU,°C]: HSSW: (34.8, −1.9); mCDW: (34.5, −1); AASW: (34.3, −0.5); MW: (0, −95.2) (Table S1 in Supporting Information S1). The MW is defined here as a "virtual" meltwater originating from subglacial melt of the RIS, following Jenkins (1999) (see Section 2.2.1). It is computed taking into account the heat fluxes involved in melting at constant pressure (enthalpy), which ensures energy conservation (see Section 2.2.1). We prefer to employ "virtual" MW instead of ISW, as done in Budillon et al. (2003), because ISW is already the product of mixing of ambient water in the RIS cavity with meltwater (Table S1 in Supporting Information S1); therefore it doesn't have specific temperature and salinity, which makes it unsuitable to be used as a fixed endpoint.

The selected endpoints are in agreement with the oceanographic measurements carried out in the framework of the Ross Ice Shelf project over 1976–1979 (Jacobs et al., 1985), the Climatic Long-term Interactions for the Mass balance in Antarctica project, over 1994–2004 (CLIMA, Budillon et al., 2003), and those published by Russo et al. (2011), who merged the World Ocean Database 2001 with the CLIMA project databases.

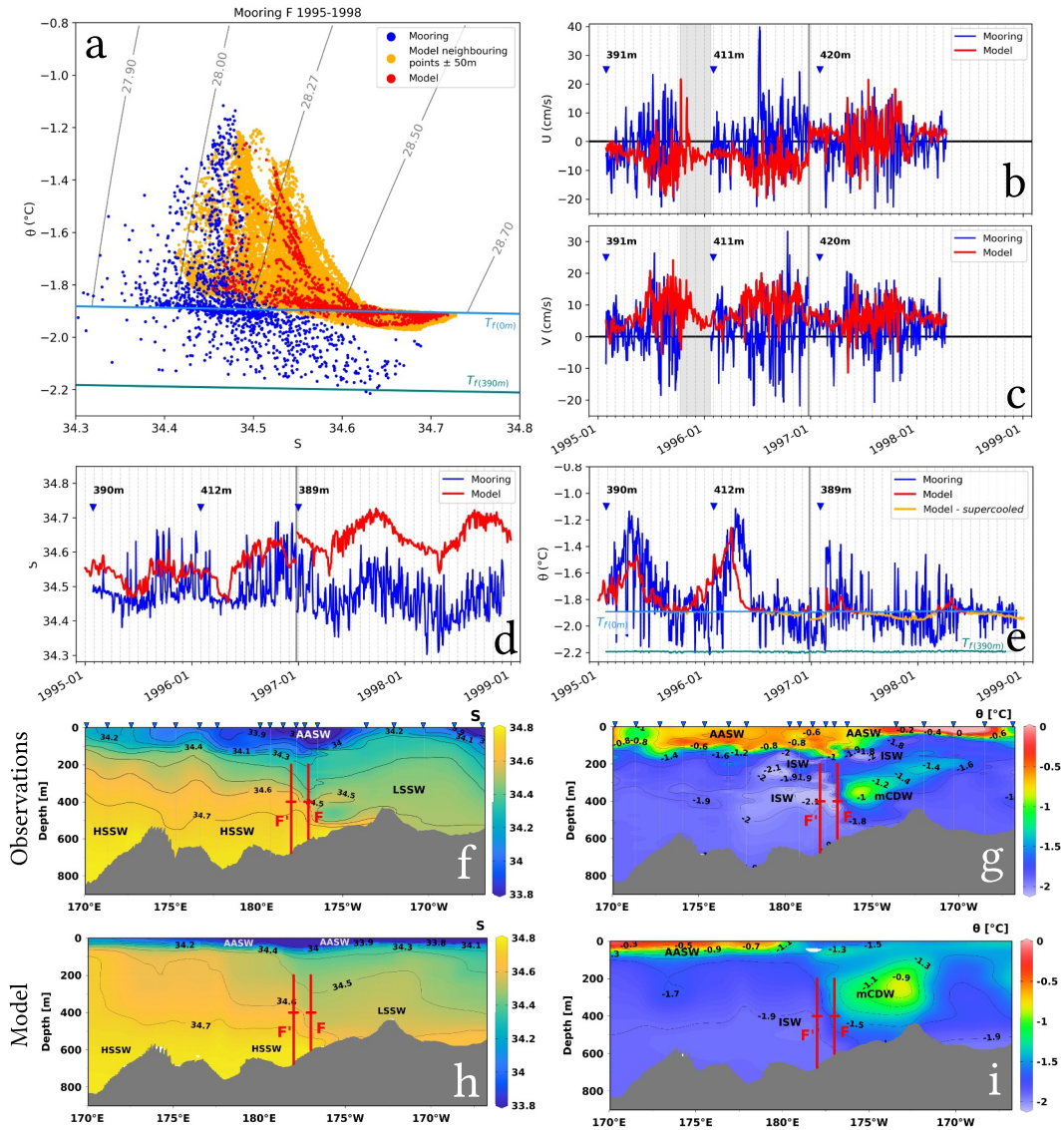

Figure 3. (a–e) Model (red) versus observations (blue) comparison, interpolated at daily frequency, at mooring F (before 1997) and F′ (after 1997), at 390 m depth in front of Ross Ice Shelf (RIS) (see location in Figure 1a). (a) θ, S plot with contours of neutral density anomaly; red: pointwise comparison, orange: neighboring grid points, at depth ±50 m of the depth of mooring F, F′. (b) Zonal velocity, (c) meridional velocity, (d) salinity, (e) potential temperature. The gray shade in (b, c) indicates the period when the mooring currentmeters stopped working. The gray line in (b–e) marks the repositioning of the mooring F to F′ location. (f–i) Conductivity-Temperature-Depth measurements of salinity (f) and temperature (g) in a section along the RIS front (CLIMA experiment January 1995); the point of view is from the inside of the cavity toward the open ocean. (h, i) Same quantities as in (f) and (g), but simulated over the same period. The mooring position and sensor depth are indicated in red in (f–i).

The calculation of the mixing ratios in its most general form is a linear system of 3 equations, each with N terms, one for each endpoint:

$$\begin{cases} m_1\theta_1 + m_2\theta_2 + \cdots + m_N\theta_N = \theta \\ m_1 S_1 + m_2 S_2 + \cdots + m_N S_N = S \\ m_1 + m_2 + \cdots + m_N = 1, \end{cases} \tag{1}$$

which represents the linear decomposition of a water mass sample of salinity S and potential temperature θ in terms of the endpoints in each grid point. The third equation represents the constraint that the sum of the mixing ratios must equal one. The Equation system 1 was already implemented in Python (https://ocefpaf.github.io/python4oceanographers/blog/2014/03/24/watermass/) for three water masses and solved by applying a linear solver. We generalized the existing method by increasing the number of endpoints to four (or more) water masses, HSSW, mCDW, AASW, and MW, by implementing a non-linear solver (see Text S4 in Supporting Information S1). However, we simplified the problem into two different three-equation systems for two separate regions: the region near Ross Island (Figure 1a), where mCDW is not simulated, and the rest of the RIS, where, conversely, AASW presence under the RIS is very limited (see Section 5), and negligible in terms of basal melting. The system that we solve is in the form:

$$\begin{cases} m_1\theta_1 + m_2\theta_2 + m_3\theta_3 + m_4\theta_4 = \theta \\ m_1 S_1 + m_2 S_2 + m_3 S_3 + m_4 S_4 = S \\ m_1 + m_2 + m_3 + m_4 = 1, \end{cases} \tag{2}$$

with $m_1 = m_{HSSW}$, $m_2 = m_{AASW}$, $m_3 = m_{mCDW} \equiv 0$, $m_4 = m_{MW}$ in the Ross Island region, and with $m_1 = m_{HSSW}$, $m_2 = m_{AASW} \equiv 0$, $m_3 = m_{mCDW}$, $m_4 = m_{MW}$ and in the rest of the RIS. The simplification, thus, is a reduction of unknowns from four to three in the two distinct regions by setting $m_{mCDW} \equiv 0$ in the Ross Island region, and $m_{AASW} \equiv 0$ in the rest of the RIS. The separation in the two regions is also necessary to avoid the intersection of the mixing lines between HSSW and AASW, with the endpoint mCDW (see, e.g., Figures 6c and 6e). Intersecting mixing lines would yield a wrong mixing calculation, as the linear system would decompose the sample water mass with the nearest endpoint, in this case, mCDW, instead of the correct mixing of HSSW and AASW. This is a limitation of using only (θ, S) properties of the endpoints. Therefore, to study regions where both AASW and mCDW are present, more specific constraints are needed to separate the mixing lines. This potentially underestimates the abundance of AASW, which has been observed to weakly intrude elsewhere along the RIS front, and on the other hand, can overestimate the abundance of mCDW.

In our case, (θ, S) in Equation system 2 are the potential temperature and salinity simulated at each ocean grid cell in contact with the ice shelf base, schematically represented by the blue dot in Figure 2. The system is in the form: $Am = b$, with the mixing rate m subject to a lower and upper boundary of 0 and 1, respectively. A is the matrix composed of the (θ_i, S_i) endpoints, m is the solution array, and b is the array with the simulated (θ, S). The solution is the array of the monthly mixing ratios m_1 to m_4 at each ocean grid cell at the RIS draft. We calculate the solution by inverting the matrix A, with the constraints on the solution array already mentioned, utilizing the `scipy.optimize.lsq_linear` function.

Notice that the endpoints' properties are fixed in time. Therefore, every change in the mixing ratios decomposition is attributable only to changes in the proportions with respect to these fixed constituents. This is necessary, as we want to highlight time changes in the relative abundance of the endpoint water masses in each sample water mass. Including time-varying endpoints would hinder the interpretation of the results. It would potentially mask the changes in relative abundance: for example, if simulated HSSW freshens/becomes more saline and we modify the endpoint salinity to match the change, we may lose most of the freshening/salinification signal in the mixing ratio of the time-varying HSSW endpoint, as the sample water masses with a strong HSSW component would also experience a similar change in properties. In analyzing long-term changes in the mixing ratios, however, it would be necessary to update the endpoints with the average (θ, S) over that time.

The total amount of basal melting of the RIS, B_{tot}, can be calculated by integrating the freshwater flux, FW_{flux}, over the entire RIS area, $B_{tot} = \int_{RIS} FW_{flux}\, dS$. By integrating the product of the freshwater flux and the mixing ratio m_i, relative to the ith water mass, we can quantify the amount of basal melting caused by that specific water mass, B_i (Equation 3), obtaining a partitioning of the basal melting:

$$B_i = \int_{RIS} \left(m_i \cdot FW_{flux}\right) dS. \tag{3}$$

The partitioned basal melt allows to: [a] quantify the average contribution of each water mass to basal melt; [b] analyze the basal melt depth distribution in relation to the depth at which the different water masses are in contact with the ice shelf; [c] analyze the time variability of basal melt in relation to the relative abundance/presence of the different water masses in contact with the ice shelf.

We also calculated the relative contribution α_i, of each water mass to basal melt:

$$\alpha_i = \frac{B_i}{B_{tot}} = \frac{1}{B_{tot}} \int_{RIS} \left(m_i \cdot FW_{flux}\right) dS. \tag{4}$$

Conceptually, this operation is also the inverse of what was done for the B_i; that is, it is the same as weighted-averaging the mixing ratios with the basal melt rate and normalizing by the total integrated basal melt. This was done in order to more closely quantify the temporal variability of the abundance of each water mass and associate it with the changes in the relative contribution of each water mass to basal melting.

2.2.1. The "Virtual" Meltwater

In the MITgcm, MW is injected in a sub-ice shelf boundary layer during melting (Losch, 2008), with salinity $S_{MW} = 0$ and potential temperature at the in situ seawater freezing point $\theta_f\ (p, S)$; p is the local pressure and S the salinity of the ambient water. However, potential temperature is not a conserved quantity like salinity and specific energy during melting. Therefore, following Jenkins (1999), a "virtual" meltwater is defined by computing the heat fluxes involved in melting at constant pressure, which ensures energy (enthalpy) conservation. The calculation is shown in Equation 5 for a unit mass of melted ice, and accounts for: (a) heat conducted in the ice column to raise the ice temperature from a nominal temperature T_i in the interior (far-field temperature) to the temperature of the ice-ocean interface, the in situ melting point $\theta_f\ (S,p)$; (b) the latent heat produced by the change of phase of ice during melting, absorbed by the ice shelf:

$$\theta_{mw} = \theta_f(S,p) - \frac{L}{c_w} - \frac{c_i}{c_w}\left(\theta_f(S,p) - T_i\right) \tag{5}$$

Here, L is the latent heat of fusion ($3.34{\cdot}10^5$ J/kg), and c_i and c_w are the specific heat capacity of ice (2,000 J/kg/K) and seawater (3,994 J/kg/K) at constant pressure. The resulting θ_{mw} is in the range $-94.95 < \theta_{mw} < -94.57$°C over a depth range [0, 1,000] m, for $S = 34$ and $T_i = -15$°C, as used for other ice shelves (Silvano et al., 2017). The depth of 1,000 m is an upper limit for the depth of the grounding line of the RIS (Fretwell et al., 2013). Employing a saltier $S = 35$ and colder $T_i = -20$°C yields $-95.2 < \theta_{mw} < -94.6$°C. This latter value of T_i is closer to the measured upper-layers ice temperature of the RIS, between [−20, −25]°C measured at J9 site (location Figure 1a, Clough & Hansen, 1979) and similarly in the Filchner-Ronne ice shelf (Grosfeld & Thyssen, 1994). Given the low relative change in $\theta_{mw}$with a change in salinity and depth, we adopted the lowest value of −95.2°C for θ_{mw}.

3. Model-Data Comparison

3.1. Water Masses

To check whether or not our MITgcm implementation led to robust simulation of the Ross Sea water masses, we compared our results with measurements from four mooring stations of the Italian Marine Observatory in the Ross Sea (MORSea, Bergamasco et al., 2002; Budillon et al., 2011; Castagno et al., 2019; Russo et al., 2011): mooring G (Drygalski Trough), H1 (Glomar Challenger Trough), H3 (continental slope, Glomar Challenger sector) and F (RIS front, moved to F′ in 1997). We compared our simulation with (θ, S) properties from CTD casts on the continental shelf collected over 1997–2006 in the course of the Climatic Long-term Interactions for the Mass balance in Antarctica (CLIMA) project and the AnSlope project in 2004. We also used measurements from expendable bathythermograph (XBT) and Conductivity-Temperature-Depth (CTD) taken along the RIS front during several past oceanic cruises in the framework of the Italian Antarctic Research Program (PNRA) and the CLIMA projects (Budillon et al., 2003). The variables compared include potential temperature, salinity, zonal and meridional velocities at daily frequency. The water masses' characteristics on the continental shelf are consistent with long-term observations from CLIMA and AnSlopeIII (Figures S3a and S3b in Supporting Information S1).

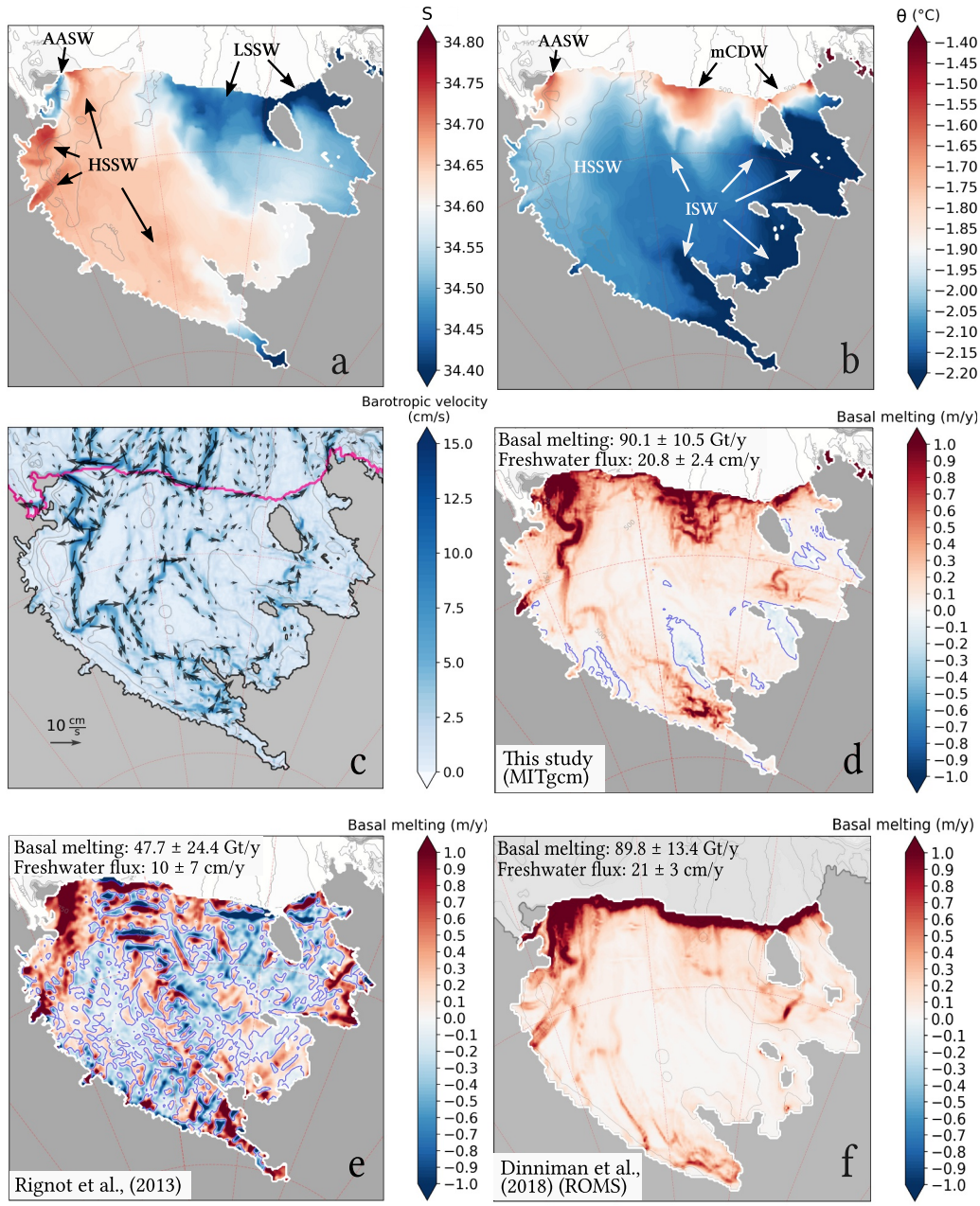

Figure 4. Simulated mean-annual fields at the Ross Ice Shelf draft, averaged over 1993–2018: (a) salinity; (b) potential temperature (°C); (c) barotropic currents (cm/s), (d) basal melting (m/yr). (e) Mean annual basal melting averaged over 1979–2010 after Rignot et al. (2013). The blue line in (d) and (e) indicates the contour of net average basal melt = 0 (f) Simulated mean annual basal melting with ROMS averaged over 1999–2015 (Dinniman et al., 2018). The magenta line in (c) indicates the ice sheet edge.

The average barotropic circulation (Figure 4c, Figure S2 in Supporting Information S1) and the vertical structure over the main troughs (Figure S5 in Supporting Information S1) are consistent with other models (Dinniman et al., 2018; Jendersie et al., 2018) and observations. Since observations are scarce for the RIS cavity, we focus on the comparison over mooring F (and F′) and the RIS front, which is the region where heat and salt exchanges take place between the open continental shelf and the cavity. For a comparison with the other moorings, see Text S5 in Supporting Information S1. Despite the scarcity of direct observations, we compared the θS properties from the location where existing borehole measurements of the RIS cavity were obtained (red triangles in Figure 1a): near Ross Island at CH-1,2 (C. L. Stewart et al., 2019), in the central part of the RIS, at HWD-2 (Stevens et al., 2020),

and close to the grounding line in Siple Coast, at WGZ (Begeman et al., 2018), KIS1 (Lawrence et al., 2023) and KIS2 (Horgan et al., 2025). These comparisons are reported in detail in Text S6 in Supporting Information S1, together with direct estimates of basal melt rates.

3.2. Mooring F

This mooring was placed near the RIS central front (Figure 1a) to study the outflows of *supercooled* Ice Shelf Water (ISW) and was active in 1995–1998. It was moved westward 25 km to the new location F′ in summer 1997 to better capture the ISW plumes. The instrument was located at a depth of ∼400 m, the depth of ISW outflows and mCDW inflows.

The properties of the water masses at mooring F and F′ are shown in the θ, S plot (Figure 3a) for both simulations and observations. In comparison with observations (blue dots), our simulations show a positive salinity bias as well as a weakened ISW plume. The high salinity tail of the modeled water masses reaches the neutral density of $\gamma_n \simeq 28.70$ kg/m^3 and is slightly (<0.05°C) *supercooled*, that is, below the surface freezing point (cyan line in Figure 3a). Several temperature measurements within the observed water masses were 0.2–0.3°C below the freezing point. The blue line around −2.2°C indicates the in situ freezing point, estimated at the depth of the mooring F, 400 m (e.g., Figure 3f), which also corresponds roughly to the RIS draft close to the mooring; this shows the melting potential of nearly all water masses observed. Mixing with mCDW is simulated well as shown by the temperature maximum and the bell-shaped scatter plot, with the warmest points lying in the range of $28.0 < \gamma_n < 28.27$ kg/m^3.

Compared to observations, the model is able to reproduce the mean temperature averaged over a few days as well as the seasonal cycle (Figure 3e). The inter-daily variability, however, is largely missing since it likely results from the astronomical tides, which are not included in our numerical setup. Mooring F measured inflows of mCDW, as periodically observed in previous campaigns (Jacobs et al., 1970, 1979; Jacobs & Giulivi, 1999). Simulated mCDW intruding at the RIS front shows warm peaks of ∼−1.3°C, about 0.6°C higher than the surface freezing point (∼−1.8°C), and ∼1°C higher than the in situ freezing point (∼−2.2°C) (Figure 3e). The mooring measured peaks of ISW with strong inter-daily variability, which are not well captured in the simulation due to the excessive mixing with ambient water, and potentially due to a lack of tidal forcing. Simulated meridional velocity (Figure 3c) indicates that outflows are mostly occurring at mooring F, whereas the mooring observations show higher variability in the occurrences of inflows and outflows. Simulated zonal velocity (Figure 3b) is mostly negative before 1997 and oscillates around zero afterward, reflecting the location change. The simulated westward and northward flow of both mCDW and ISW is consistent with the steering of both the inflows and outflows across the RIS front due to the ice shelf draft. The smaller-scale dynamics occurring at the RIS front are difficult to capture, probably because of grid resolution, and potentially also because of long-term changes in the RIS geometry, due to the advance or retreat of the ice shelf front, or calving events, which are not represented in the model boundary conditions. Moreover, the smaller inter-daily variability of simulated velocities, compared to observations, could be potentially impacted by the missing diurnal tides. Tides have been shown, both in observation and model studies, to produce strong jets along the RIS as topographically trapped vorticity waves (MacAyeal, 1984b; Padman et al., 2003). On the other hand, our model may reproduce partially trapped topographic Rossby waves, as shown in previous studies (MacAyeal, 1984a). Simulated salinity shows a salty bias of ∼0.1 (F location) and ∼0.15 (F′ location); however, the seasonal variability is captured (Figure 3d). The bias is probably inherited from the reanalysis GLORYS12V1, which shows a bias of +0.75°C in temperature and of ∼+0.2 PSU in salinity in the open ocean (upper 2,000 m) in the first years of the reanalysis. In the later years of reanalysis, which coincide with the ARGO period (1999–2019), the bias is reduced to 0.45°C and 0.1 PSU, respectively.

3.3. Sections Along RIS Front

Simulated salinity is in good agreement with observations from CLIMA, especially in the deeper layer westward of 175°W (cf. Figures 3f and 3h, the portion of the section between the left edge and mooring F). The model correctly represents the salinity gradient between the western and eastern portions of the cavity, which is well documented in observations (Jacobs et al., 1970; Orsi et al., 1999). Higher salinity than observed is simulated in the intermediate layers, and in particular in the deep layer of the eastern part of the section (eastward of 175°W), which may represent either an expanded HSSW in the eastern cavity or be related to the potential salinity bias

10.1029/2025JC023103

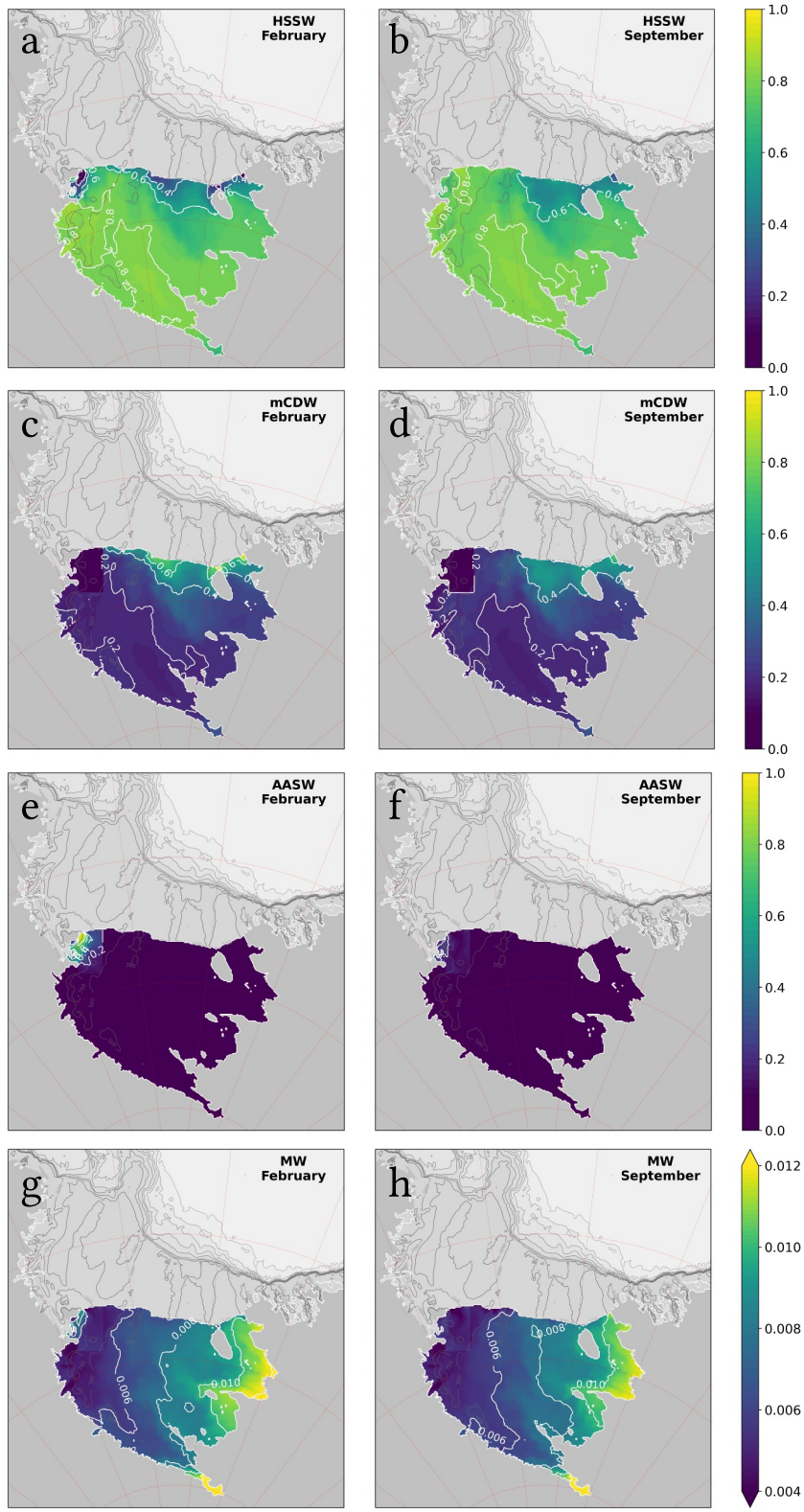

Figure 5. Calculated monthly mixing ratios for the water masses (endpoints in Table S1 in Supporting Information S1), averaged over 1993–2018: (a, b) High Salinity Shelf Water, (c, d) modified Circumpolar Deep Water, (e, f) Antarctic Surface Water; (g, h) Meltwater. The months reported (February and September) are representative of the late austral summer and the peak of winter, respectively.

already reported (Figure 3h). Along Hayes Bank, at ∼172°W, we simulated mCDW inflows, at a similar temperature to the observed one, with the mCDW core slightly displaced eastward and upward (cf. Figures 3g and 3i). The plume of ISW in the simulation shows a weaker low-temperature extreme than observed, which is likely due to excessive mixing of the water masses, given the model resolution. AASW temperature and salinity are similar in both the model and observations. Simulated AASW eastward of 180°W in the transect are about 1.3°C colder than observed (−1.3°C simulated vs. ∼0°C obs., Figures 3g and 3i). The comparison also shows that the model simulates a thinner halocline and thermocline than observed, probably due to the coarse z-levels at the surface or a more compact sea ice cover that inhibits turbulence. A comparison with a similar XBT transect along RIS made in February 2017 (PNRA 2017 campaign OGS Explora) shows similar discrepancies between our simulation and the observations (Figures S7a and S7b in Supporting Information S1). The discrepancies between the simulated and observed mCDW temperature in sections 1995 and 2017 can be caused by a different timing of the peak of the intrusion in the simulation compared to the observations. Intrusions as warm as those simulated were indeed measured by mooring F in 1995 and 1996 (Figure 3e). Previous observations confirm that mCDW as warm as simulated in this study have indeed occurred in this sector of the RIS front (Jacobs et al., 1970; Jacobs & Giulivi, 1999; Smethie & Jacobs, 2005). The wider simulated core of mCDW could also be caused by the lack of tidal forcing (Jendersie et al., 2018) or by excessive mixing induced by the use of the GMREDI eddy parameterization. Comparison with vmADCP-measured zonal and meridional velocities during the 2017 expedition shows that currents along the front are generally underestimated in our model (Figure S6 in Supporting Information S1), as well as currents variability, as in mooring F (Figures 3b and 3c). Missing tidal components, which were not implemented in our model, are thought to strengthen flow along the RIS by the generation of topographic Rossby waves (MacAyeal, 1984a) and may explain the discrepancy.

Due to the more compact and persistent sea ice cover, observations from the eastern Ross Sea are very scarce and limited to CTD samples collected during early summer. Therefore, observations may not capture the full intrusion of CDW. Overall, the comparison with the mooring and the CTD section shows that the simulated water masses are found at locations and depths that are consistent with observations (Figures 3f–3i). The water masses are simulated with properties that are consistent with the observations (Figure 3a) and with reasonable dynamics, despite the absence of tidal forcing.

4. Results: RIS Basal Melt

4.1. Basal Melt: Model-Data Comparison

Simulated basal melting (Figure 4d) exhibits a spatial pattern that is inherently related to the different water masses that circulate in the RIS cavity (Figures 4a–4c): high melting near the front is mostly due to simulated mCDW, advected along the Hayes Bank, Houtz Bank, and the Little America Basin, and simulated AASW, heated during summer and advected into the cavity near Ross Island (simulated AASW does not reach under the RIS strongly in any other sector). The western part of the cavity undergoes relatively high melting due to simulated HSSW (Figures 4a and 4d). By contrast, the central and eastern portions of the cavity, where HSSW is not strongly present, exhibit generally low melting. Refreezing occurs near the grounding line and in the central part of the RIS. The depth distribution of water masses at the RIS draft, averaged over the RIS area, confirms that the most widespread water mass is HSSW (Figure S11b in Supporting Information S1), found in the layers deeper than −200 m, followed by mCDW found mostly between −200 − −400 m, and AASW, only found in the shallowest part (>−300 m).

We compared our simulated mean-annual basal melt with that from Rignot et al. (2013), who used an indirect data-model approach to infer the melt rates (cf. Figures 4d and 4e). The latter is an average for the period 1979–2010, based on indirect satellite observations of ice velocities, simulated surface mass balance, and simulated flux calculations from ice sheet models to calculate the basal mass budget. As such, and given the fact that the basal melting of the RIS is relatively low with respect to other ice shelves, it is subject to a large uncertainty. It does not show a clear spatial pattern, except for higher values along the RIS front and along the grounding line (as simulated, in particular for the Western cavity along the Ross Island), and patches of strong refreezing. Although the high melting near the front and the grounding line in Rignot et al. (2013) is consistent with our numerical model, features such as the alternating areas of high melting and refreezing are missing, which are likely artifacts of their methodology. Simulated refreezing, however, lacks frazil ice formation, which would significantly increase the amount of refreezing taking place (Jenkins & Bombosch, 1995; Smedsrud & Jenkins, 2004). The

simulated basal melting integrated over the RIS, averaged over 1993–2018 (the time span of our simulation), is 90.1 ± 10.5 Gt/yr, twice as high as the estimate of Rignot et al. (2013), 47.7 ± 24.4 Gt/yr. Simulated basal melting estimates, like ours, tend to be higher than observed ones (see Table S2 in Supporting Information S1). Our simulated basal melting is, however, in line with other model-based studies (e.g., Dinniman et al., 2018; Kusahara & Hasumi, 2013; Mack et al., 2019; Naughten et al., 2018; Richter et al., 2020) (Table S2 in Supporting Information S1).

A different model of the Ross Sea based on ROMS (Dinniman et al., 2018), run from 1999 to 2015, yields similar results in terms of average melt: 90 ± 10 (MITgcm) versus 90 ± 13 Gt/yr (ROMS). The pattern of basal melting is very similar to ours, simulated with the MITgcm (cf. Figures 4d and 4f). The distribution and attribution show some differences: in ROMS, the whole RIS front is impacted by AASW, with strengthening in the Ross Island region, whereas in the MITgcm, only the latter region is affected (Figure S13 in Supporting Information S1). AASW is likely overrepresented in ROMS, due to ice shelf draft smoothing that is necessary with sigma-coordinates (terrain-following). Strong localized intrusions of mCDW into the RIS cavity are also present in Dinniman et al. (2018), but the mCDW core is simulated at a depth much larger than the RIS draft in the region of the intrusion(not shown). This diminishes the amount of mCDW in contact with the ice shelf, strongly decreasing the interaction with the ice shelf base. The higher impact of AASW in ROMS than in the MITgcm simulation results in the stronger seasonal cycle of melting (see Figure S13g in Supporting Information S1). See more details of the comparison between the two models in Text S7 in Supporting Information S1.

The more recent observation-based estimate of Adusumilli et al. (2020), averaged over the period 2010–2018, yields 80 ± 82 Gt/yr, which shows good agreement with our simulated value. Their observed melting depth-distribution is consistent with our simulated one (Figure S11a in Supporting Information S1). Simulated basal-melting depth distribution shows refreezing occurring at 300–350 m depth and melting occurring mostly as deep as 750 m in the range of ~ 1 Gt $y^{-1}m^{-1}$. Most of the melting, however, is distributed at the depth of the RIS front, 200–350 m, which is not observed in Adusumilli et al. (2020). The discrepancy is likely caused by the particularly warm mCDW in our simulation, which is nevertheless consistent with observations and measurements from nearby mooring F, as discussed in the previous section. Notice that the high relative error in the integrated melt rates in Adusumilli et al. (2020) makes their estimate compatible with 0 at a 95% confidence level, which is indicative of the high uncertainty of any indirectly derived estimate of basal melting. In their work, Adusumilli et al. (2020) show a long-term basal melting variability at only two locations in the Ross Sea: the Byrd Glacier and the Ross Island region. Our simulated melting rate at Byrd Glacier reaches a maximum value of 3.5 m/yr, which is only about half that in Adusumilli et al. (2020), possibly because of underestimated current strength locally, due to model grid resolution, or alternatively because of the large subglacial meltwater that takes place there, but is not included in the boundary conditions of our model (Stearns et al., 2008). Conversely, our simulation yields 6.5 m/yr in the Ross Island region, which is 3 times higher than their value (Figure 4d). Melting in the Ross Island region is, however, consistent with the simulated and observed water masses, since it is influenced by both warm AASW, which yields high melting, and HSSW, while Byrd glacier is impacted by HSSW only.

A detailed comparison of the available observations of basal melting and ocean properties under the RIS is reported in Text S6 in Supporting Information S1.

4.2. Mixing Ratios and Partitioned Basal Melt

The mixing ratios obtained with the method described in Section 2.2, for the water masses in contact with the RIS draft (Figure 5), reveal similarities to the maps of temperature and salinity (Figures 4a and 4b). This means that the mixing ratios correctly represent the proportions of the characteristic water masses (endpoints) inside the cavity for each grid point.

A monthly climatology averaged over 1993–2018 shows the seasonal changes in the distribution of basal melting of the RIS in the (θ, S) space (Figure 6). Basal melting is locally high in the austral summer months (January–March) (Figures 6c, 6e, and 6g), consistent with localized intrusions of warm AASW (−0.5°C, 34.3) and its mixing with HSSW (−1.9°C, 34.8). Melting by HSSW is strengthened in the austral winter months (Figures 6d–6f and 6h). Melting by relatively warm mCDW (−1°C, 34.5), which enters the central-eastern RIS cavity and weakly mixes with HSSW, is also strengthened during the summer (Figures 6a, 6c, 6e, and 6g), although residual melting remains in the winter months as well (Figures 6b, 6d, 6f, and 6h). The area near the

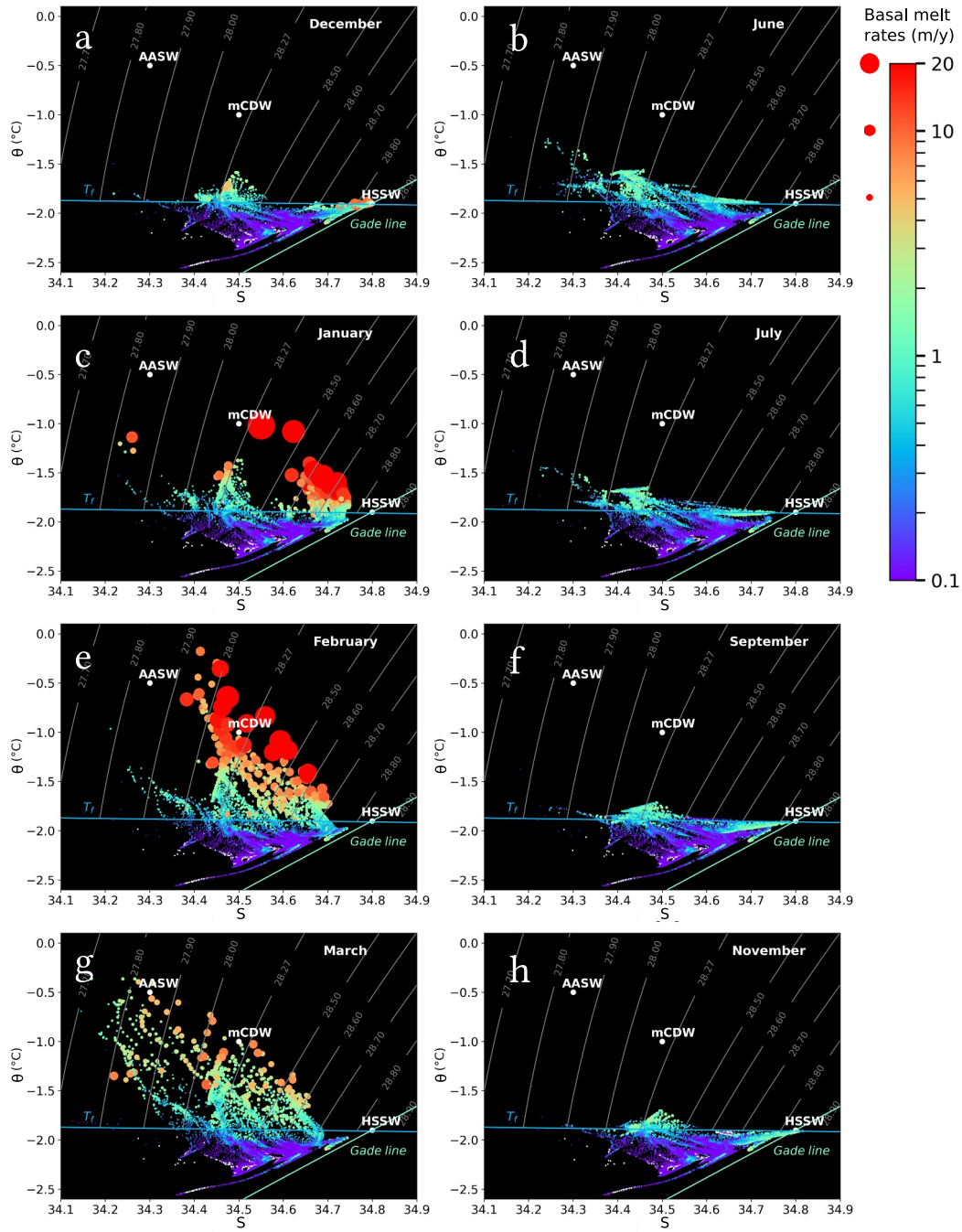

Figure 6. Distribution in the (θ, S) space of the simulated water masses at the ice shelf draft grid points; color and size of the dots correspond to the value of basal melting at the grid points (monthly averaged over 1993–2018). White dots indicate net refreezing occurrences. Mixing with meltwater is represented by a single "Gade line" (Gade, 1979; Wåhlin et al., 2010), plotted in green, departing from High Salinity Shelf Water. T_f indicates the surface freezing point. Gray contours show neutral density anomaly.

grounding line corresponds to the coldest portion of the graph ($T \sim -2.2$°C), where basal melting rates are low, and refreezing occurs locally (white dots). The scatter plot highlights: (a) the presence of summer "modes" associated with AASW and mCDW and a "winter" mode associated with HSSW; (b) the mixing of water masses inside the cavity, which acts to spread the θ, S properties between the fixed endpoints; (c) the effect of the cavity, which cools and freshens by mixing water masses with MW along "Gade lines" (Gade, 1979; Wåhlin et al., 2010).

The western part of the RIS base is mostly in contact with HSSW (Figures 5a and 5b), which reaches more than 90% mixing ratio in austral winter (June–September) due to polynyas activity near the RIS front, but remains high, also during summer (January to March), at 80% mixing ratio. The HSSW mixing ratio also remains high in the eastern portion of the RIS, with values above 60%.

mCDW is brought along the Hayes Bank, Houtz Banks, and Little America Basin (Jacobs et al., 1979, 1985; Smethie & Jacobs, 2005) and penetrates into the RIS cavity through a large sector of the central and eastern RIS front (Figures 5c and 5d). There, the mixing ratio of mCDW reaches 40% in summer and 20% in winter. AASW intrudes near Ross Island (Figures 5e and 5f), reaching a maximum mixing ratio of about 40% in the late summer (February to March) in agreement with observations by C. L. Stewart et al. (2019), and almost disappears during the winter season. At the peak of the intrusion, it reaches up to 120 km below the RIS before losing its heat signature. We observe other small intrusions along the western RIS, caused by the AASW wedge, but in those regions, AASW reaches only up to 20 km into the RIS, causing far less melting. The halted polynyas activity in summer, which causes a water column stratification, induces a nearly horizontal tilt of the isopycnals at the RIS front, thus allowing mCDW and AASW to reach the cavity in our simulation. MW has the lowest relative mixing ratios (Figures 5g and 5h): the maximum mixing ratio of ∼0.1‰ is reached from February to April near Ross Island, following the seasonal melting pulse produced by AASW. High values are also found along the grounding line in Gould Coast and Marie Byrd Land, reaching 0.008‰.

The predominant melting contributor is the HSSW (Figures 5a and 5b), which accounts on average for 68% of total RIS melting over 1993–2018. A similar calculation yields 25% for mCDW (Figures 5c and 5d), and 7% for AASW (Figures 5e and 5f), while melting associated with MW is negligible (<0.001%, Figures 5g and 5h). MW has the role of representing the effect of the melting ice shelf on the ocean water masses and provides an endpoint for the mixing analysis that is not associated with basal melting. It was, therefore, not considered in the analysis.

4.3. Temporal Variability of Basal Melt

The total integrated basal melting of the RIS (Figure 7a) shows a superposition of phenomena with different periodicities: a long-term oscillation over the whole simulation time and interannual variability, superimposed on the seasonal cycle. The partitioning method described in Section 2.2 shows how different water masses are affected by processes at different time scales. Following Equation 3, and to increase readability, basal melt induced by HSSW, mCDW, and AASW will be referred to as B_{HSSW}, B_{mCDW}, B_{AASW}, respectively, in the following (Figure 7b).

The climatology over 1993–2018 (Figure 7e) shows that the seasonal cycle of B_{HSSW} is weak, less than 10 Gt/yr in amplitude, and shows double relative peaks: one in March, representative of summertime circulation speed up, and a larger one in June, caused by wintertime salinification due to brine rejection. The seasonal cycle of B_{mCDW} is about double that of B_{HSSW} (∼20 Gt/y) and peaks in March to May, the austral fall. This is later than the intrusions observed in the austral summer in Castagno et al. (2017) and Y. Wang et al. (2023), because of the time it takes for mCDW to circulate from the continental shelf to the RIS front. The strengthening of B_{mCDW} is caused by increased intrusions of CDW along the continental shelf break, potentially caused by seasonal weakening of the ASF and increased intrusions into the RIS cavity. We hypothesize that the latter is caused by the increased stratification during summer close to the RIS front, related to the temporary lack of brine formation, which reduces the isopycnals tilt near the RIS front. B_{AASW} exhibits a strong seasonal cycle of ∼25 Gt/yr amplitude, which peaks in February and is absent during the winter season, consistent with C. L. Stewart et al. (2019). While observations have shown that AASW is able to reach sub-ice shelf environments in some areas (Malyarenko et al., 2019; C. L. Stewart et al., 2019), the physical pathways and controls of this exchange remain largely unknown.

B_{HSSW} ranges from ∼40 Gt/yr to ∼70 Gt/yr (Figure 7b). After removing the time average over the whole simulation period (1993–2018) and the seasonal cycle, B_{HSSW}, shows a single multi-decadal oscillation, with an initial phase of growing (1993–2003), a short stationary phase (2003–2005), a second growth (2005–2008) and then a decrease until 2016, and a final surge in 2017 (Figure 7c). Overall interannual variability of B_{HSSW} is small (Figure 7c). B_{mCDW} shows a similar trend to B_{HSSW} over 1993–2006, but then exhibits a sharp increase in 2007–2008, and a gradual decrease in the following years of the simulation (Figure 7b). B_{mCDW} ranges from ∼15 Gt/yr to ∼50 Gt/yr (Figure 7b) and exhibits a larger interannual variability than B_{HSSW} (Figure 7c). B_{AASW} does not have a trend; it is mostly present in the summer months (January to March), where it ranges generally from less

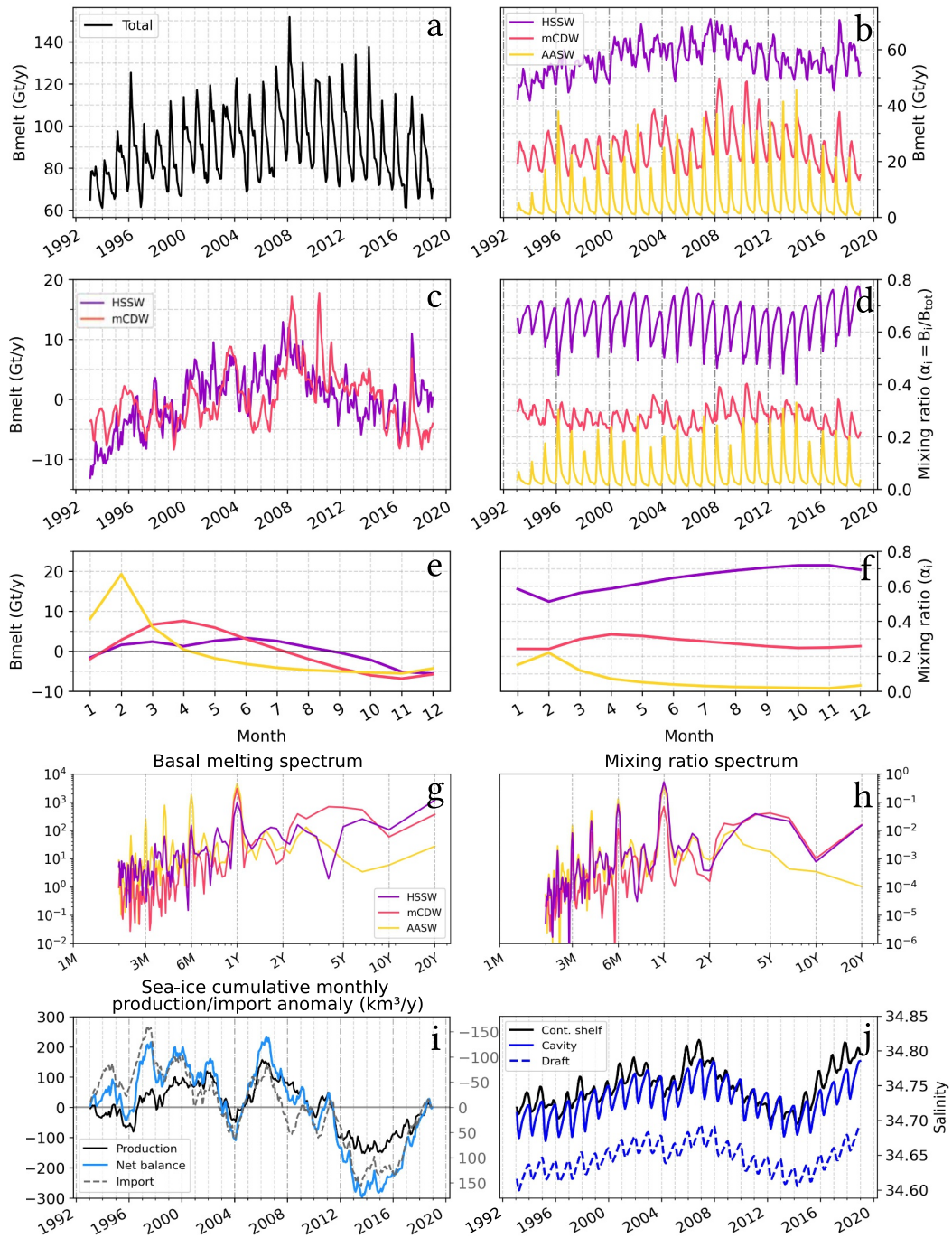

Figure 7. (a) Monthly total Ross Ice Shelf (RIS) basal melting. (b) Monthly RIS basal melting partitioned by each endpoint: High Salinity Shelf Water (HSSW, purple), modified Circumpolar Deep Water (mCDW, orange), and Antarctic Surface Water (yellow). (c) Same as (b) for HSSW and mCDW, but as the anomaly around the multiyear monthly mean. (d) Basal melting fraction ($\alpha_i = B_i/B_{tot}$), coinciding with basal-melting weighted mixing ratios (Equation 4). (e) Seasonal cycle of basal melting anomaly, that is, the multiyear monthly anomaly around the multiyear mean. (f) Multiyear monthly mean of α_i. (g) Power spectrum density of the monthly basal melting, partitioned into the specific water masses. (h) Same as (g) for the basal melting fraction. The strong peak at 1 yr is the seasonal cycle. (i) Cumulative-time integral of the monthly sea-ice production anomaly $\left(\mathrm{km}^3/\mathrm{y}\right)$ in polynyas (solid black) compared to the imported sea ice into the eastern Ross Sea continental shelf (gray dash, reversed *y*-axis) and the net anomaly (light blue). See Section 4.4 for more details. (j) Salinity average over the open continental shelf, the RIS cavity, and RIS draft, west of 180°E.

than ~20 Gt/yr to 40 Gt/yr (Figure 7b). The interannual variability of B_{AASW}, specifically considering the summer maxima, is high.

The seasonal cycle of the melting-weighted mixing ratios, that is, the fractional basal melting α_i (Equation 4), is shown in Figure 7f. It shows that the mixing ratios of the warm water masses (AASW, mCDW) reach their minima and maxima around the year almost synchronously to the basal melting in Figure 7e, while the mixing ratio of HSSW shows a different behaviour. α_{AASW} is high in the summer (maximum 0.2 in February) and is negligible in the other seasons. α_{mCDW} is similarly high during late summer (March to May). α_{HSSW} shows differences from the melt variability, with a strong minimum in February, which abruptly reverses to increasing values during the autumn and winter seasons, reaching a maximum in October to November, consistent with the analysis of Yan et al. (2023) for the western Ross Ice Shelf Polynya. This increase is related to the wintertime salinification of the western RIS cavity, while the minimum in February is caused by the temporary occurrence of AASW near Ross Island, which displaces HSSW from the base of the ice shelf. The correlations between the relative partitioned melting (Figure 7f) show that α_{HSSW} is negatively correlated with both α_{AASW} ($r = -0.84$, $p < 0.01$) and α_{mCDW} ($r = -0.37$, $p < 0.01$), indicating that HSSW alternates with mCDW and AASW in causing melting.

Analyzing the long-term changes (Figure 7d), we notice a mostly stationary contribution of HSSW from 1993 to 2006, with values of α_{HSSW} around 0.7 on average, but minima and maxima ranging from 0.4 to ~0.8. The summer minima are synchronous with maxima of α_{AASW}. The α_{HSSW} shifts to a negative trend from 2006 to 2014, when it reverts to positive until 2018. The α_{mCDW} starts with a slightly decreasing trend, experiences local maxima in 2003–2004, and shows an opposite trend with respect to HSSW in the 2006–2018 period. Minima and maxima range from 0.2 to 0.4. Finally, the α_{AASW} shows a behavior strongly resembling B_{AASW}. Minima are near 0 during wintertime, although summertime maxima range between 0.15 and 0.3.

The power distribution of the B_i and α_i variability is quantified in the periodograms (Figures 7g and 7h), and confirms that: (a) the seasonal variability is the strongest periodicity for all water masses, especially for mCDW and AASW; (b) interannual variability is strongest for mCDW and second for HSSW, and it peaks between 2.5 and 7 years. Notice that for periods longer than ~10 years, the power spectrum is unreliable because the window length is comparable to the simulation time span. The B_i and α_i spectra are similar, although we notice some discrepancies: the spectrum of B_{HSSW} shows a dip in the basal melt spectrum at 4 years, which is absent in the spectrum of α_{HSSW}; the spectrum of B_{AASW} shows a different behavior in the longer period section than the spectrum of α_{AASW}.

4.4. Impact of Sea-Ice Variability on Basal Melt

Recent studies point to sea ice production and sea ice import from the Amundsen Sea as major drivers of the salinity of HSSW in the Ross Sea (Castagno et al., 2019; Silvano et al., 2020). The simulated sea ice production and import are in the order of 100 km^3 yearly, which makes it an important contribution to the continental shelf waters' salinity. We computed sea ice production/import monthly anomalies with respect to our model climatology, and added the anomalies to compute a monthly cumulative sea-ice production/import anomaly curve (Figure 7i). The details of the computation are reported in Text S8 in Supporting Information S1. Sea ice import is calculated by accounting for the sea ice entering the eastern Ross Sea in a 100-km long section, extending from the Edward VII Peninsula toward the continental shelf break. Sea-ice production is computed in the locations where polynyas are observed: the Terra Nova Bay polynya in the western Ross Sea (Figure 1a), the McMurdo polynya near Ross Island, and the Ross Ice Shelf polynya in front of the ice shelf. The cumulative sum of monthly anomalies helps us understand how an imbalance in the salinity caused by anomalous sea ice import or sea ice production can stay in the system and affect the salinity of the water masses on the continental shelf (Figure S14e in Supporting Information S1). In particular, the salinity anomaly of the HSSW can be transferred to the RIS cavity within the timeframe of circulation. To understand the impact of sea ice production on salinity, we compared the anomalous cumulative curve with the average salinity on the western Ross Sea continental shelf, with the average salinity in the western part of the RIS cavity and with the salinity at the western RIS draft (Figure 7j, where by western we mean all the area west of the 180°E line). The cumulative anomaly of sea ice production correlates with the average salinity on the western continental shelf, cavity, and RIS draft; the

correlations are at $r = 0.49$, $p < 0.01$, $r = 0.49$, $p < 0.01$, and $r = 0.58$, $p < 0.01$, respectively. Notice that we adopt a simpler approach than the more detailed budget in Yan et al. (2023), as we don't partition salinity into upper, middle, and lower layers. Overall, we are not interested in the quantification of salinity fluxes, but in analyzing the time behavior of sea ice, salinity, and basal melting by HSSW.

There is some moderate correlation ($r = -0.44$, $p < 0.01$) between sea ice import and sea ice production cumulative anomalies (Figure 7i). This indicates that the freshwater import at the eastern boundary of the Ross Sea can affect the salinity balance in the rest of the Ross Sea by modulating sea ice production. We find a weak correlation between basal melting by HSSW and salinity ($r < 0.3$); however, the correlation is higher if we consider α_{HSSW}, which correlates with the salinity of the RIS at $r = 0.57$, $p < 0.01$. Despite the low correlation, the salinity signal is partially reflected in the basal melting signal (cf. Figures 7j, 7b, and 7d), with rising periods between 1993 and 2008, a decline until 2014, followed by a rebound, and temporary minima during 1996 and 2003–2004. The fact that the correlations with basal melting are moderate may be explained by the number of processes taking place that reduce the coherence of the signals, and the slow circulation and large residence time of water masses inside the cavity, which may offset the signals. In fact, cavity circulation time of HSSW is estimated to be around 3.5 years (with chlorofluorocarbons, Smethie & Jacobs, 2005) or in the range 5.5–7.5 years (with stable isotopes and noble gases, Loose et al., 2009).

The simulated annual sea-ice formation (Figure S14g in Supporting Information S1) compares well with satellite-derived quantities, measured with microwave radiometers, employed for a similar analysis in Silvano et al. (2020) (cf. their extended data, Figure 3b with Figure S14g in Supporting Information S1 here). Despite the similarity there is some mismatch during some years (2000, 2004, 2007, 2010), which may be explained, at least in the first two cases, by the presence of large tabular icebergs in the Glomar Challenger Trough (Arrigo et al., 2002), which were not included in the model forcing; icebergs may affect circulation and also sea ice production by creating temporarily polynyas. Second, a slightly different period definition for computing annual averages was employed in Silvano et al. (2020), where they considered each year spanning from November to October; they also computed sea ice production from satellite over the RIS and TNB polynyas separately and over the whole continental shelf. We included the McMurdo polynya and excluded the months when sea-ice net melting occurs, typically from November to February, in the simulation.

These findings suggest that the RIS cavity is a slow-responding environment to processes occurring on the continental shelf and on the eastern boundary. The type of ASF, "dense" or "cold" in the Ross Sea, also plays an important role in shielding the continental shelf from direct changes occurring in the open ocean (Thompson et al., 2018). In the simulation, we observe a strong variability in the transport strength of the Ross Sea gyre, which does not reflect on the continental shelf and cavity circulation strength (Figures S14a and S14b in Supporting Information S1) or on the water masses properties (Figures S14e and S14f in Supporting Information S1).

Our model simulated a widespread salinity rebound in 2014–2018, which appears in α_{HSSW} (Figure 7d), in B_{HSSW} (Figure 7c), and in the cumulative sea ice production anomaly (Figure 7i). Annual sea ice import and production, however, showed little change in 2014, where the net sea ice anomaly budget is near zero, although in the later years it is consistently positive (Figure S14g in Supporting Information S1). Our model does not reproduce the freshening trend observed during the last decades, and the reason probably lies either in the salty bias in the upper 2,000 m from the boundary conditions (GLORYS12V1, Lellouche et al., 2021), amounting to 0.2 PSU, or in the higher simulated sea ice production (see Text S8 in Supporting Information S1). Alternatively, it may be caused by atmospheric forcing (ERA5, Hersbach et al., 2020), which may explain the generally higher-than-observed simulated sea ice production or also missing freshwater fluxes in the model setup, such as icebergs. This may introduce discrepancies in the comparison with the observed impact of teleconnections.

5. Discussion

5.1. Applicability of the Method

The method shown here employs seawater physical properties (temperature and salinity) to characterize basal melt, allowing the study of its variability in relation to each water mass type. A distinction between "cold" and "warm" modes has already been made by Mack et al. (2019). They distinguished the two modes based on whether or not the seawater temperature at the ice shelf draft is above or below the surface freezing point (a "supercooling

criterion"). Comparing our results (Figures 7a and 7b) with those obtained with the "supercooling criterion" (Figure S12 in Supporting Information S1), we see that in the latter, the decadal variability of basal melt is largely missing. Such differences may introduce interpretation biases of spatio-temporal variability in "cold" cavities, assigning most of the long-term variability to "warm" modes.

Most parameterizations of ice shelf basal melt, used in ice sheet–ice shelf models to project multicentennial sea-level change, do not take into account a realistic oceanographic setting, except for the thermal forcing, which is usually extrapolated inside the cavities. It is applied either as a linear term (Martin et al., 2011) or a quadratic term, to account for turbulence-induced overturning (Pollard & DeConto, 2012). More advanced parameterizations simulate a buoyancy-driven overturning (Pelle et al., 2019; Reese et al., 2018), and may apply a correction factor to tune the strength of the overturning in each Antarctic sector, but are still relying on extrapolated water masses properties, and using it and tuning it are problematic where multiple water masses are present, for example, in the larger "cold" cavities. A new procedure used in the Ice Sheet Model Intercomparison Project phase 6 (ISMIP6), which accounts for extrapolated oceanic conditions and employs the quadratic melting parameterizations of Pollard and DeConto (2012), was developed in Favier et al. (2019) and Jourdain et al. (2020). They developed a local (point-wise) and non-local (whole ice-shelf wide) quadratic formulation of basal melting, which extrapolates observations over the continental shelf into the ice shelf cavities. Jourdain et al. (2020) achieved a statistical calibration procedure for tuning the parameters at a pan-Antarctic level by using Rignot et al. (2013) results (Figure 4e). Both points raise problems because of the scarcity of data coverage for the continental shelf and because the basal melt map of Rignot et al. (2013) is strongly affected by observational biases and large uncertainty. This makes the ISMIP6 procedure not fully reliable in low-melting, multi-modal cavities. All these parameterizations are able to reproduce existing behavior, but do not fully capture the dynamics of ocean circulation and processes occurring on the continental shelf. This then contributes to the high uncertainty of long-term ice sheet projections in the past or future, or, in case ocean properties change drastically, may lead to unrealistic results.

The present work shows that it is possible to use oceanographic data to separate the different components of basal melting. The use of mixing ratios removes the need to separate melting occurring at specific depths (Jacobs et al., 1992) and allows tracking water masses while they mix as they circulate in the cavity. This is useful in "multimodal cavities," and may be applied to ice sheet–ice shelf models for tuning each melting mode separately. Partitioned basal melting could be extremely useful in the context of regime shifts, when long-term sustained ocean changes on the continental shelf can alter the melting "modes" of the ice shelves drastically. For example, the potential change from "fresh" to "warm" on the eastern side of continental shelves where large "cold" cavities are located, as simulated by ocean models (Hellmer et al., 2012; Naughten et al., 2021). It is important to notice that the method relies on the definition of properties of the water masses, which may change drastically, for example, during glacial cycles, or on multicentennial projections, but could nonetheless be identified in the (θ, S) plots. The emergence of coupled climate–ice sheet models (Siahaan et al., 2022) is a great tool to study thresholds and regime shifts in the sub-ice shelf cavities. However, they may not accurately represent water mass properties due to large biases caused by the misrepresentation of localized oceanic processes like polynyas and DSW formation. This makes it necessary to develop techniques to distinguish water masses causing melting, to evaluate, and to identify thresholds and timing of melting regime shifts.

The analysis carried out suggests that the properties of the water masses are not the only drivers of basal melting; in fact, the α_i are not strictly mirroring the B_i. The other factor that comes into play in the three-equation formulation is the strength of currents, which would translate to more turbulence and higher heat and salinity fluxes. However, this was not addressed in the present paper and will be the subject of further work.

5.2. Limitations

Mixing ratios are difficult to compare with observations, which are extremely scarce beneath large ice shelf cavities (e.g., Arzeno et al., 2014; Begeman et al., 2018; Falco, Krauzig, et al., 2024; Gilmour, 1979; Jacobs et al., 1979; Lawrence et al., 2023; Michel et al., 1979; Marsh et al., 2016; C. L. Stewart et al., 2019; Stevens et al., 2020; Whiteford et al., 2022). The method relies on the careful assignment of the endpoints, which need to be in line with both observations (e.g., Budillon et al., 2003; Jacobs et al., 1985) and with the simulated water masses. Therefore the model needs to be able to accurately reproduce the main physical properties (salinity,

temperature) of seawater. Care must be taken in avoiding endpoints that overlap with mixing lines of other endpoints, as this would give wrong results from a wrong distance calculation in the (θ, S) space. In our case, this was solved by regionally subsetting the area near Ross Island, where AASW, HSSW, and MW were employed (to avoid the possible overlapping of mCDW and the AASW-HSSW mixing line), and the rest of the cavity, where HSSW, mCDW, and MW were employed. This limitation could be relaxed by including chemical tracers such as oxygen or oxygen isotopes to track specific water masses (as in Jenkins, 1999; Silvano et al., 2017, 2018), and help distinguish the oxygen-depleted CDW, from the oxygen-enriched AASW, and better identify the δ^{18}O-depleted glacial meltwater. Silica, phosphates, and nitrates, together with chlorofluorocarbons, may highlight water masses conversion rates inside the cavity (Smethie & Jacobs, 2005). Lagrangian tracers could be used to study the variability of single parcels of water interacting with the ice shelf or to track MW as it originates in the RIS cavity. The water masses partitioning method was recently applied to the borehole measurements at the Kamb Ice Stream grounding zone, employing as endpoints HSSW, subglacial discharge water, and glacial meltwater (Horgan et al., 2025; Washam et al., 2023), or just HSSW and glacial meltwater (Lawrence et al., 2023).

The model does a reasonable job of simulating the observed water masses and sea ice. Despite this, we note a few discrepancies. The surface layer in the RIS front section of 1995 and 2017 shows excessive warmth, as well as a sharp thermocline located at ∼100 m. By comparison, observations show a finer pattern of warmer and cooler waters and a deeper thermocline at ∼170 m depth. The sections also show that the model simulated a wider intrusion of mCDW reaching the RIS front and weak ISW plumes. These issues are likely related to the model representation of mixing and the eddy-permitting (not "resolving") resolution, unable to resolve the mesoscale and to resolve in detail vertical mixing processes in the near-surface layer. Comparison with mooring data shows that time variability is lower in the model, and simulated currents are generally weaker. This could be related to missing tides in the model or weaker winds in the ERA5 reanalysis. Some of the biases present in salinity and temperature could also be inherited by GLORYS12V1 reanalysis, used as lateral open boundary conditions, where they have been documented.

Other limitations are specific to our ocean modeling framework: missing tides, which are an important component of across-shelf transport of DSW and CDW (Padman et al., 2009, 2018), and a driver of circulation in the RIS shallow portions near the grounding line (MacAyeal, 1984b). Tides are known to stir the water column near the grounding line, especially along Siple Coast, increasing vertical mixing and ultimately basal melting, and to affect the exchanges along the RIS. A more energetic circulation near the grounding line would produce higher melting, which would be attributed mostly to HSSW. As for the RIS front exchanges, a comparison with models that include tides in the literature shows that tides cause a smaller core of mCDW to intrude over Hayes and Houtz Bank. The lack of tides, therefore, potentially overestimates the abundance of mCDW and its contribution to basal melting. Overall, it is possible that our assumptions and limitations are overestimating the contribution of mCDW, and slightly underestimating the contribution of AASW and HSSW. However, these biases are static and would produce an offset in the mean values, rather than different time and space variability. Other limitations include: non-interactive ice shelf, which can alter the boundary conditions of the RIS front, and are important for comparison with satellite-based observations; hydrostaticity which does not allow to simulate specific small-scale processes of DSW cascading at the shelf break, or the AASW wedge (Malyarenko et al., 2019) in the deeper portions of the RIS front; model resolution, both vertical and horizontal which does not allow to properly resolve small-scale features, such as convective plumes near the grounding line and mesoscale dynamics (the latter, however, does not appear to be a key driver of RIS basal melting, Mack et al., 2019); model resolution also hampers the ability to capture small-scale internal wave processes at the RIS front (MacAyeal, 1984a; Padman et al., 2003). Model parameters are not well constrained under a large cavity due to the lack of observations, and therefore, we may not capture some potentially important mixing processes, for example, due to interactions with waves induced by the topography or the ice shelf morphology. Finally, despite its importance for ice dynamics, the grounding line is particularly difficult to model properly, as evidenced by comparison with borehole observations. This is due to the proximity to hydrological systems that are difficult to include in a model setup, and due to complex ice shelf draft morphology (Begeman et al., 2018; Horgan et al., 2025; Lawrence et al., 2023; Washam et al., 2023), with channels and crevasses that strongly impact localized basal melting, and that would require specific parameterizations in order to be accounted for (Marsh et al., 2016; Price et al., 2025; Whiteford et al., 2022).

6. Conclusions

In this work, we simulated the transient oceanic circulation in the Ross Sea and in the cavity beneath the Ross Ice Shelf (RIS), with a new implementation of the MITgcm numerical model at 5-km horizontal resolution. A mixing-ratio decomposition was developed and applied to the simulated water masses circulating in the Ross Ice Shelf cavity for the period 1993–2018, in order to analyze their spatio-temporal variability and their contribution to basal melting. (a) Simulated basal melting of the Ross Ice Shelf is 90 Gt/yr on average, and is partitioned into High Salinity Shelf Water (HSSW), (68%), modified Circumpolar Deep Water (mCDW), (25%), and Antarctic Surface Water (AASW), (7%); the RIS meltwater is included as an endpoint but does not account for any melting. (b) The different time scales of basal melt variability arise differently for each water mass, from seasonal to decadal. The AASW and mCDW express a strong seasonal cycle, whereas the decadal variability is mostly highlighted in the HSSW. Interannual variability is stronger for the mCDW. (c) The variability of basal melting from the HSSW is mostly related to the salinity of the HSSW that enters the cavity, which is enhanced by sea ice production in polynyas and on the continental shelf, and reduced by sea ice and freshwater imported into the Eastern Ross Sea; however, low correlation values indicate that other processes are at play, which were not clearly identified. The decadal and interannual variability of basal melting depends on the long-term properties of water masses, whose abundance and dynamics are potentially related to tropical teleconnections.

Conflict of Interest

The authors declare no conflicts of interest relevant to this study.

Data Availability Statement

The simulated output necessary to reproduce the analysis is uploaded on figshare with DOI: https://doi.org/10.6084/m9.figshare.24285976.

Acknowledgments

Funding: This work was supported mainly by the Italian Minister of Education, University and Research (MIUR), by the National Institute for Oceanography and Applied Geophysics (OGS), with funding from the Italian National Programme for Antarctic Research (PNRA) "ANTIPODE" (PI Dr. Florence Colleoni) Grant PNRA18_00002 and the High Performance Computing Training and Research for Earth Sciences" (HPC-TRES) Grant 2022-03. *HPC Resources*: The simulations were carried out in the CINECA supercomputing infrastructures (GALILEO, MARCONI100), through the Italian SuperComputing Resource Allocation (ISCRA) initiative (IscraB PALEOMIT, IscraC DEGLAMIT).

References

Adusumilli, S., Fricker, H. A., Medley, B., Padman, L., & Siegfried, M. R. (2020). Interannual variations in meltwater input to the Southern Ocean from Antarctic ice shelves. *Nature Geoscience*, *13*(9), 616–620. https://doi.org/10.1038/s41561-020-0616-z

Arrigo, K. R., van Dijken, G. L., Ainley, D. G., Fahnestock, M. A., & Markus, T. (2002). Ecological impact of a large Antarctic iceberg. *Geophysical Research Letters*, *29*(7), 8-1–8-4. https://doi.org/10.1029/2001gl014160

Arzeno, I. B., Beardsley, R. C., Limeburner, R., Owens, B., Padman, L., Springer, S. R., et al. (2014). Ocean variability contributing to basal melt rate near the ice front of Ross Ice Shelf, Antarctica. *Journal of Geophysical Research: Oceans*, *119*(7), 4214–4233. https://doi.org/10.1002/2014jc009792

Begeman, C. B., Tulaczyk, S. M., Marsh, O. J., Mikucki, J. A., Stanton, T. P., Hodson, T. O., et al. (2018). Ocean stratification and low melt rates at the Ross Ice Shelf grounding zone. *Journal of Geophysical Research: Oceans*, *123*(10), 7438–7452. https://doi.org/10.1029/2018jc013987

Bergamasco, A., Ardizzon, G., Carniel, S., Meloni, R., & Sclavo, M. (2004). The Ross Shelf cavity water exchange variability during 1995-1998. *Il Nuovo Cimento - C*, *27*(3), 241–254.

Bergamasco, A., Defendi, V., Zambianchi, E., & Spezie, G. (2002). Evidence of dense water overflow on the Ross Sea shelf-break. *Antarctic Science*, *14*(3), 271–277. https://doi.org/10.1017/s0954102002000068

Budillon, G., Castagno, P., Aliani, S., Spezie, G., & Padman, L. (2011). Thermohaline variability and Antarctic bottom water formation at the Ross Sea shelf break. *Deep Sea Research Part I: Oceanographic Research Papers*, *58*(10), 1002–1018. https://doi.org/10.1016/j.dsr.2011.07.002

Budillon, G., Cordero, S. G., & Salusti, E. (2002). On the dense water spreading off the Ross Sea shelf (Southern Ocean). *Journal of Marine Systems*, *35*(3–4), 207–227. https://doi.org/10.1016/s0924-7963(02)00082-9

Budillon, G., Pacciaroni, M., Cozzi, S., Rivaro, P., Catalano, G., Ianni, C., & Cantoni, C. (2003). An optimum multiparameter mixing analysis of the shelf waters in the Ross Sea. *Antarctic Science*, *15*(1), 105–118. https://doi.org/10.1017/s095410200300110x

Castagno, P., Capozzi, V., DiTullio, G. R., Falco, P., Fusco, G., Rintoul, S. R., et al. (2019). Rebound of shelf water salinity in the Ross Sea. *Nature Communications*, *10*(1), 1–6. https://doi.org/10.1038/s41467-019-13083-8

Castagno, P., Falco, P., Dinniman, M. S., Spezie, G., & Budillon, G. (2017). Temporal variability of the Circumpolar Deep Water inflow onto the Ross Sea continental shelf. *Journal of Marine Systems*, *166*, 37–49. https://doi.org/10.1016/j.jmarsys.2016.05.006

Clough, J. W., & Hansen, B. L. (1979). The Ross ice shelf project. *Science*, *203*(4379), 433–434. https://doi.org/10.1126/science.203.4379.433

Das, I., Padman, L., Bell, R. E., Fricker, H. A., Tinto, K. J., Hulbe, C. L., et al. (2020). Multidecadal basal melt rates and structure of the Ross Ice Shelf, Antarctica, using airborne ice penetrating radar. *Journal of Geophysical Research: Earth Surface*, *125*(3), e2019JF005241. https://doi.org/10.1029/2019jf005241

Depoorter, M. A., Bamber, J., Griggs, J., Lenaerts, J. T., Ligtenberg, S. R., van den Broeke, M. R., & Moholdt, G. (2013). Calving fluxes and basal melt rates of Antarctic ice shelves. *Nature*, *502*(7469), 89–92. https://doi.org/10.1038/nature12567

Dinniman, M. S., Klinck, J. M., Bai, L.-S., Bromwich, D. H., Hines, K. M., & Holland, D. M. (2015). The effect of atmospheric forcing resolution on delivery of ocean heat to the Antarctic floating ice shelves. *Journal of Climate*, *28*(15), 6067–6085. https://doi.org/10.1175/jcli-d-14-00374.1

Dinniman, M. S., Klinck, J. M., Hofmann, E. E., Smith, J., & Walker, O. (2018). Effects of projected changes in wind, atmospheric temperature, and freshwater inflow on the Ross Sea. *Journal of Climate*, *31*(4), 1619–1635. https://doi.org/10.1175/JCLI-D-17-0351.1

Dinniman, M. S., Klinck, J. M., & Smith, W. O. (2003). Cross-shelf exchange in a model of the Ross Sea circulation and biogeochemistry. *Deep Sea Research Part II: Topical Studies in Oceanography*, *50*(22), 3103–3120. https://doi.org/10.1016/j.dsr2.2003.07.011

Dinniman, M. S., Klinck, J. M., & SmithJr, W. O. (2007). Influence of sea ice cover and icebergs on circulation and water mass formation in a numerical circulation model of the Ross Sea, Antarctica. *Journal of Geophysical Research*, *112*(C11). https://doi.org/10.1029/2006jc004036

Dinniman, M. S., Klinck, J. M., & SmithJr, W. O. (2011). A model study of Circumpolar Deep Water on the West Antarctic Peninsula and Ross Sea continental shelves. *Deep Sea Research Part II: Topical Studies in Oceanography*, *58*(13–16), 1508–1523. https://doi.org/10.1016/j.dsr2.2010.11.013

Falco, P., Aulicino, G., Castagno, P., Capozzi, V., de Ruggiero, P., & Garzia, A. (2024). Ocean-atmosphere-ice processes in the Ross Sea: A review. *Deep Sea Research Part II: Topical Studies in Oceanography*, 105429.

Falco, P., Krauzig, N., Castagno, P., Garzia, A., Martellucci, R., Cotroneo, Y., et al. (2024). Winter thermohaline evolution along and below the Ross Ice Shelf. *Nature Communications*, *15*(1), 1–10. https://doi.org/10.1038/s41467-024-54751-8

Favier, L., Jourdain, N. C., Jenkins, A., Merino, N., Durand, G., Gagliardini, O., et al. (2019). Assessment of sub-shelf melting parameterisations using the ocean–ice-sheet coupled model NEMO (v3. 6)–Elmer/Ice (v8. 3). *Geoscientific Model Development*, *12*(6), 2255–2283. https://doi.org/10.5194/gmd-12-2255-2019

Fretwell, P., Pritchard, H. D., Vaughan, D. G., Bamber, J. L., Barrand, N. E., Bell, R., et al. (2013). Bedmap2: Improved ice bed, surface and thickness datasets for Antarctica. *The Cryosphere*, *7*(1), 375–393. https://doi.org/10.5194/tc-7-375-2013

Gade, H. G. (1979). Melting of ice in sea water: A primitive model with application to the Antarctic ice shelf and icebergs. *Journal of Physical Oceanography*, *9*(1), 189–198. https://doi.org/10.1175/1520-0485(1979)009<0189:moiisw>2.0.co;2

Gille, S. T. (2002). Warming of the Southern Ocean since the 1950s. *Science*, *295*(5558), 1275–1277. https://doi.org/10.1126/science.1065863

Gilmour, A. (1979). Ross Ice Shelf sea temperatures. *Science*, *203*(4379), 438–439. https://doi.org/10.1126/science.203.4379.438

Grosfeld, K., & Thyssen, F. (1994). Temperature investigation and modeling on the Filchner-Ronne Ice Shelf, Antarctica. *Annals of Glaciology*, *20*, 377–385. https://doi.org/10.1017/s0260305500016724

Gwyther, D. E., Spain, E. A., King, P., Guihen, D., Williams, G. D., Evans, E., et al. (2020). Cold ocean cavity and weak basal melting of the sørsdal ice shelf revealed by surveys using autonomous platforms. *Journal of Geophysical Research: Oceans*, *125*(6), e2019JC015882. https://doi.org/10.1029/2019jc015882

Haumann, F. A., Gruber, N., Münnich, M., Frenger, I., & Kern, S. (2016). Sea-ice transport driving southern ocean salinity and its recent trends. *Nature*, *537*(7618), 89–92. https://doi.org/10.1038/nature19101

Hellmer, H. H., Kauker, F., Timmermann, R., Determann, J., & Rae, J. (2012). Twenty-first-century warming of a large Antarctic ice-shelf cavity by a redirected coastal current. *Nature*, *485*(7397), 225–228. https://doi.org/10.1038/nature11064

Hellmer, H. H., & Olbers, D. J. (1989). A two-dimensional model for the thermohaline circulation under an ice shelf. *Antarctic Science*, *1*(4), 325–336. https://doi.org/10.1017/s0954102089000490

Hersbach, H., Bell, B., Berrisford, P., Hirahara, S., Horányi, A., Muñoz-Sabater, J., et al. (2020). The ERA5 global reanalysis. *Quarterly Journal of the Royal Meteorological Society*, *146*(730), 1999–2049. https://doi.org/10.1002/qj.3803

Holland, P. R., Jenkins, A., & Holland, D. M. (2008). The response of ice shelf basal melting to variations in ocean temperature. *Journal of Climate*, *21*(11), 2558–2572. https://doi.org/10.1175/2007jcli1909.1

Holland, P. R., & Kwok, R. (2012). Wind-driven trends in Antarctic Sea-Ice drift. *Nature Geoscience*, *5*(12), 872–875. https://doi.org/10.1038/ngeo1627

Horgan, H. J., Stewart, C. L., Stevens, C., Dunbar, G., Balfoort, L., & Schmidt, B. E. (2025). A West Antarctic grounding-zone environment shaped by episodic water flow. (pp. 1–7). Nature geoscience.

Jacobs, S., Amos, A. F., & Bruchhausen, P. M. (1970). Ross Sea oceanography and Antarctic bottom water formation. *Deep-Sea Research and Oceanographic Abstracts*, *17*(6), 935–962. https://doi.org/10.1016/0011-7471(70)90046-x

Jacobs, S., Fairbanks, R. G., & Horibe, Y. (1985). Origin and evolution of water masses near the Antarctic continental margin: Evidence from $ \text{H}_{2}^{\mythinspace 18}$ O / $\text{H}_{2}^{\mythinspace 16}$O ratios in seawater. *Oceanology of the Antarctic Continental Shelf*, *43*, 59–85.

Jacobs, S., & Giulivi, C. (1999). Thermohaline data and ocean circulation on the Ross Sea continental shelf. In *Oceanography of the Ross Sea Antarctica* (pp. 3–16). Springer.

Jacobs, S., Giulivi, C., & Dutrieux, P. (2022). Persistent Ross Sea freshening from imbalance west Antarctic ice shelf melting. *Journal of Geophysical Research: Oceans*, *127*(3), e2021JC017808. https://doi.org/10.1029/2021jc017808

Jacobs, S., Giulivi, C., & Mele, P. (2002). Freshening of the Ross Sea during the late 20th century. *Science*, *297*(5580), 386–389. https://doi.org/10.1126/science.1069574

Jacobs, S., Gordon, A. L., & Ardai, J., Jr. (1979). Circulation and melting beneath the Ross Ice Shelf. *Science*, *203*(4379), 439–443. https://doi.org/10.1126/science.203.4379.439

Jacobs, S., Helmer, H., Doake, C., Jenkins, A., & Frolich, R. (1992). Melting of ice shelves and the mass balance of Antarctica. *Journal of Glaciology*, *38*(130), 375–387. https://doi.org/10.3189/s0022143000002252

Jendersie, S., Williams, M. J., Langhorne, P. J., & Robertson, R. (2018). The density-driven winter intensification of the Ross Sea circulation. *Journal of Geophysical Research: Oceans*, *123*(11), 7702–7724. https://doi.org/10.1029/2018jc013965

Jenkins, A. (1999). The impact of melting ice on ocean waters. *Journal of Physical Oceanography*, *29*(9), 2370–2381. https://doi.org/10.1175/1520-0485(1999)029<2370:tiomio>2.0.co;2

Jenkins, A., & Bombosch, A. (1995). Modeling the effects of frazil ice crystals on the dynamics and thermodynamics of ice shelf water plumes. *Journal of Geophysical Research*, *100*(C4), 6967–6981. https://doi.org/10.1029/94jc03227

Jenkins, A., Dutrieux, P., Jacobs, S., Steig, E. J., Gudmundsson, G. H., Smith, J., & Heywood, K. J. (2016). Decadal ocean forcing and Antarctic ice sheet response: Lessons from the Amundsen Sea. *Oceanography*, *29*(4), 106–117. https://doi.org/10.5670/oceanog.2016.103

Jenkins, A., Hellmer, H. H., & Holland, D. M. (2001). The role of meltwater advection in the formulation of conservative boundary conditions at an ice–ocean interface. *Journal of Physical Oceanography*, *31*(1), 285–296. https://doi.org/10.1175/1520-0485(2001)031<0285:tromai>2.0.co;2

Jones, J. M., Gille, S. T., Goosse, H., Abram, N. J., Canziani, P. O., Charman, D. J., et al. (2016). Assessing recent trends in high-latitude Southern Hemisphere surface climate. *Nature Climate Change*, *6*(10), 917–926. https://doi.org/10.1038/nclimate3103

Jourdain, N. C., Asay-Davis, X., Hattermann, T., Straneo, F., Seroussi, H., Little, C. M., & Nowicki, S. (2020). A protocol for calculating basal melt rates in the ISMIP6 Antarctic ice sheet projections. *The Cryosphere*, *14*(9), 3111–3134. https://doi.org/10.5194/tc-14-3111-2020

Klinck, J., & Dinniman, M. (2010). Exchange across the shelf break at high southern latitudes. *Ocean Science*, *6*(2), 513–524. https://doi.org/10.5194/os-6-513-2010

Kusahara, K., & Hasumi, H. (2013). Modeling Antarctic ice shelf responses to future climate changes and impacts on the ocean. *Journal of Geophysical Research: Oceans*, *118*(5), 2454–2475. https://doi.org/10.1002/jgrc.20166

Lawrence, J., Washam, P., Stevens, C., Hulbe, C., Horgan, H., Dunbar, G., et al. (2023). Crevasse refreezing and signatures of retreat observed at Kamb Ice Stream grounding zone. *Nature Geoscience*, *16*(3), 238–243. https://doi.org/10.1038/s41561-023-01129-y

Lellouche, J.-M., Greiner, E., Bourdallé-Badie, R., Garric, G., Melet, A., & Drévillon, M. (2021). The Copernicus global 1/12 oceanic and sea ice GLORYS12 reanalysis. *Frontiers in Earth Science*, *9*, 698876.

Li, X., Cai, W., Meehl, G. A., Chen, D., Yuan, X., Raphael, M., et al. (2021). Tropical teleconnection impacts on Antarctic climate changes. *Nature Reviews Earth & Environment*, *2*(10), 680–698. https://doi.org/10.1038/s43017-021-00204-5

Liu, Y., Moore, J. C., Cheng, X., Gladstone, R. M., Bassis, J. N., Liu, H., et al. (2015). Ocean-driven thinning enhances iceberg calving and retreat of Antarctic ice shelves. *Proceedings of the National Academy of Sciences*, *112*(11), 3263–3268. https://doi.org/10.1073/pnas.1415137112

Loose, B., Schlosser, P., Smethie, W., & Jacobs, S. (2009). An optimized estimate of glacial melt from the ross ice shelf using noble gases, stable isotopes, and CFC transient tracers. *Journal of Geophysical Research*, *114*(C8). https://doi.org/10.1029/2008jc005048

Losch, M. (2008). Modeling ice shelf cavities in a z coordinate ocean general circulation model. *Journal of Geophysical Research*, *113*(C8). https://doi.org/10.1029/2007jc004368

MacAyeal, D. R. (1984a). Numerical simulations of the Ross Sea tides. *Journal of Geophysical Research*, *89*(C1), 607–615. https://doi.org/10.1029/jc089ic01p00607

MacAyeal, D. R. (1984b). Thermohaline circulation below the Ross Ice Shelf: A consequence of tidally induced vertical mixing and basal melting. *Journal of Geophysical Research*, *89*(C1), 597–606. https://doi.org/10.1029/jc089ic01p00597

Mack, S. L., Dinniman, M. S., Klinck, J. M., McGillicuddy, D. J., Jr., & Padman, L. (2019). Modeling Ocean Eddies on Antarctica's cold water continental shelves and their effects on ice shelf basal melting. *Journal of Geophysical Research: Oceans*, *124*(7), 5067–5084. https://doi.org/10.1029/2018JC014688

Malyarenko, A., Robinson, N., Williams, M., & Langhorne, P. (2019). A wedge mechanism for summer surface water inflow into the Ross Ice Shelf cavity. *Journal of Geophysical Research: Oceans*, *124*(2), 1196–1214. https://doi.org/10.1029/2018jc014594

Marsh, O. J., Fricker, H. A., Siegfried, M. R., Christianson, K., Nicholls, K. W., Corr, H. F., & Catania, G. (2016). High basal melting forming a channel at the grounding line of Ross Ice Shelf, Antarctica. *Geophysical Research Letters*, *43*(1), 250–255. https://doi.org/10.1002/2015gl066612

Marshall, J., Adcroft, A., Hill, C., Perelman, L., & Heisey, C. (1997). A finite-volume, incompressible Navier Stokes model for studies of the ocean on parallel computers. *Journal of Geophysical Research*, *102*(C3), 5753–5766. https://doi.org/10.1029/96jc02775

Marshall, J., Hill, C., Perelman, L., & Adcroft, A. (1997). Hydrostatic, quasi-hydrostatic, and nonhydrostatic ocean modeling. *Journal of Geophysical Research*, *102*(C3), 5733–5752. https://doi.org/10.1029/96jc02776

Martin, M. A., Winkelmann, R., Haseloff, M., Albrecht, T., Bueler, E., Khroulev, C., & Levermann, A. (2011). The Potsdam Parallel Ice Sheet Model (PISM-PIK)–Part 2: Dynamic equilibrium simulation of the Antarctic ice sheet. *The Cryosphere*, *5*(3), 727–740. https://doi.org/10.5194/tc-5-727-2011

Mathiot, P., & Jourdain, N. C. (2023). Southern Ocean warming and Antarctic ice shelf melting in conditions plausible by late 23rd century in a high-end scenario. *Ocean Science*, *19*(6), 1595–1615. https://doi.org/10.5194/os-19-1595-2023

McPhail, S. D., Furlong, M. E., Pebody, M., Perrett, J., Stevenson, P., Webb, A., & White, D. (2009). Exploring beneath the PIG Ice Shelf with the Autosub3 AUV. In *Oceans 2009-Europe* (pp. 1–8).

McPhail, S. D., Templeton, R., Pebody, M., Roper, D., & Morrison, R. (2019). Autosub long range AUV missions under the Filchner and Ronne ice shelves in the Weddell Sea, Antarctica-an engineering perspective. In *Oceans 2019-Marseille* (pp. 1–8).

Meehl, G. A., Arblaster, J. M., Chung, C. T., Holland, M. M., DuVivier, A., Thompson, L., et al. (2019). Sustained ocean changes contributed to sudden antarctic sea ice retreat in late 2016. *Nature Communications*, *10*(1), 14. https://doi.org/10.1038/s41467-018-07865-9

Michel, R., Linick, T., & Williams, P. (1979). Tritium and carbon-14 distributions in seawater from under the Ross Ice Shelf Project ice hole. *Science*, *203*(4379), 445–446. https://doi.org/10.1126/science.203.4379.445

Moholdt, G., Padman, L., & Fricker, H. A. (2014). Basal mass budget of Ross and Filchner-Ronne ice shelves, Antarctica, derived from Lagrangian analysis of ICESat altimetry. *Journal of Geophysical Research: Earth Surface*, *119*(11), 2361–2380. https://doi.org/10.1002/2014jf003171

Morrison, A., Hogg, A. M., England, M., & Spence, P. (2020). Warm Circumpolar Deep Water transport toward Antarctica driven by local dense water export in canyons. *Science Advances*, *6*(18), eaav2516. https://doi.org/10.1126/sciadv.aav2516

Nakayama, Y., Manucharyan, G., Zhang, H., Dutrieux, P., Torres, H. S., Klein, P., et al. (2019). Pathways of ocean heat towards Pine Island and Thwaites grounding lines. *Scientific Reports*, *9*(1), 1–9. https://doi.org/10.1038/s41598-019-53190-6

Nakayama, Y., Timmermann, R., Rodehacke, C. B., Schröder, M., & Hellmer, H. H. (2014). Modeling the spreading of glacial meltwater from the Amundsen and Bellingshausen Seas. *Geophysical Research Letters*, *41*(22), 7942–7949. https://doi.org/10.1002/2014gl061600

Naughten, K. A., De Rydt, J., Rosier, S. H., Jenkins, A., Holland, P. R., & Ridley, J. K. (2021). Two-timescale response of a large Antarctic ice shelf to climate change. *Nature Communications*, *12*(1), 1–10. https://doi.org/10.1038/s41467-021-22259-0

Naughten, K. A., Meissner, K. J., Galton-Fenzi, B. K., England, M. H., Timmermann, R., Hellmer, H. H., et al. (2018). Intercomparison of Antarctic ice-shelf, ocean, and sea-ice interactions simulated by MetROMS-iceshelf and FESOM 1.4. *Geoscientific Model Development*, *11*(4), 1257–1292. https://doi.org/10.5194/gmd-11-1257-2018

Nelson, M. J., Queste, B. Y., Smith, I. J., Leonard, G. H., Webber, B. G., & Hughes, K. G. (2017). Measurements of Ice Shelf Water beneath the front of the Ross Ice Shelf using gliders. *Annals of Glaciology*, *58*(74), 41–50. https://doi.org/10.1017/aog.2017.34

Nicholls, K., Abrahamsen, E., Buck, J., Dodd, P., Goldblatt, C., Griffiths, G., et al. (2006). Measurements beneath an Antarctic ice shelf using an autonomous underwater vehicle. *Geophysical Research Letters*, *33*(8). https://doi.org/10.1029/2006gl025998

Orsi, A. H., Johnson, G. C., & Bullister, J. L. (1999). Circulation, mixing, and production of Antarctic Bottom Water. *Progress in Oceanography*, *43*(1), 55–109. https://doi.org/10.1016/s0079-6611(99)00004-x

Padman, L., Erofeeva, S., & Joughin, I. (2003). Tides of the Ross Sea and Ross ice shelf cavity. *Antarctic Science*, *15*(1), 31–40. https://doi.org/10.1017/s0954102003001032

Padman, L., Howard, S. L., Orsi, A. H., & Muench, R. D. (2009). Tides of the northwestern Ross Sea and their impact on dense outflows of Antarctic Bottom Water. *Deep Sea Research Part II: Topical Studies in Oceanography*, *56*(13–14), 818–834. https://doi.org/10.1016/j.dsr2.2008.10.026

Padman, L., Siegfried, M. R., & Fricker, H. A. (2018). Ocean tide influences on the Antarctic and Greenland ice sheets. *Reviews of Geophysics*, *56*(1), 142–184. https://doi.org/10.1002/2016rg000546

Paolo, F. S., Fricker, H. A., & Padman, L. (2015). Volume loss from Antarctic ice shelves is accelerating. *Science*, *348*(6232), 327–331. https://doi.org/10.1126/science.aaa0940

Pelle, T., Morlighem, M., & Bondzio, J. H. (2019). Brief communication: Picop, a new ocean melt parameterization under ice shelves combining pico and a plume model. *The Cryosphere*, *13*(3), 1043–1049. https://doi.org/10.5194/tc-13-1043-2019

Pollard, D., & DeConto, R. (2012). Description of a hybrid ice sheet-shelf model, and application to Antarctica. *Geoscientific Model Development*, *5*(5), 1273–1295. https://doi.org/10.5194/gmd-5-1273-2012

Price, D., Snodgrass, J., Rack, W., Purdie, H., Hulbe, C., Wild, C. T., et al. (2025). Basal reflectance and melt rates across the Ross Ice Shelf, Antarctica, from grounding line to ice shelf front. *Journal of Glaciology*, *71*, e27. https://doi.org/10.1017/jog.2025.10

Pritchard, H., Ligtenberg, S. R., Fricker, H. A., Vaughan, D. G., van den Broeke, M. R., & Padman, L. (2012). Antarctic ice-sheet loss driven by basal melting of ice shelves. *Nature*, *484*(7395), 502–505. https://doi.org/10.1038/nature10968

Reese, R., Albrecht, T., Mengel, M., Asay-Davis, X., & Winkelmann, R. (2018). Antarctic sub-shelf melt rates via pico. *The Cryosphere*, *12*(6), 1969–1985. https://doi.org/10.5194/tc-12-1969-2018

Richter, O., Gwyther, D. E., King, M. A., & Galton-Fenzi, B. K. (2020). Tidal modulation of Antarctic ice shelf melting. *The Cryosphere Discussions*, 1–32.

Rignot, E., Jacobs, S., Mouginot, J., & Scheuchl, B. (2013). Ice-shelf melting around Antarctica. *Science*, *341*(6143), 266–270. https://doi.org/10.1126/science.1235798

Rignot, E., Mouginot, J., Scheuchl, B., Van Den Broeke, M., Van Wessem, M. J., & Morlighem, M. (2019). Four decades of Antarctic Ice Sheet mass balance from 1979–2017. *Proceedings of the National Academy of Sciences*, *116*(4), 1095–1103. https://doi.org/10.1073/pnas.1812883116

Robinson, N. J., Williams, M. J., Stevens, C. L., Langhorne, P. J., & Haskell, T. G. (2014). Evolution of a supercooled Ice Shelf Water plume with an actively growing subice platelet matrix. *Journal of Geophysical Research: Oceans*, *119*(6), 3425–3446. https://doi.org/10.1002/2013jc009399

Russo, A., Bergamasco, A., Carniel, S., Grieco, L., Sclavo, M., & Spezie, G. (2011). Climatology and decadal variability of the Ross Sea shelf waters. *Advances in Oceanography and Limnology*, *2*(1), 55–77. https://doi.org/10.1080/19475721.2011.575179

Schaffer, J., Timmermann, R., Arndt, J. E., Steinhage, D., & Kanzow, T. (2014). RTopo-2: A global dataset of ice sheet topography, cavity geometry and ocean bathymetry to study ice-ocean interaction in Northeast Greenland.

Schmidt, B. E., Washam, P., Davis, P. E., Nicholls, K. W., Holland, D. M., Lawrence, J. D., et al. (2023). Heterogeneous melting near the Thwaites Glacier grounding line. *Nature*, *614*(7948), 471–478. https://doi.org/10.1038/s41586-022-05691-0

Schmidtko, S., Heywood, K. J., Thompson, A. F., & Aoki, S. (2014). Multidecadal warming of Antarctic waters. *Science*, *346*(6214), 1227–1231. https://doi.org/10.1126/science.1256117

Siahaan, A., Smith, R. S., Holland, P. R., Jenkins, A., Gregory, J. M., Lee, V., et al. (2022). The Antarctic contribution to 21st-century sea-level rise predicted by the UK Earth System Model with an interactive ice sheet. *The Cryosphere*, *16*(10), 4053–4086. https://doi.org/10.5194/tc-16-4053-2022

Silvano, A., Foppert, A., Rintoul, S. R., Holland, P. R., Tamura, T., Kimura, N., et al. (2020). Recent recovery of Antarctic Bottom Water formation in the Ross Sea driven by climate anomalies. *Nature Geoscience*, *13*(12), 780–786. https://doi.org/10.1038/s41561-020-00655-3

Silvano, A., Rintoul, S. R., & Herraiz-Borreguero, L. (2016). Ocean-ice shelf interaction in East Antarctica. *Oceanography*, *29*(4), 130–143. https://doi.org/10.5670/oceanog.2016.105

Silvano, A., Rintoul, S. R., Peña-Molino, B., Hobbs, W. R., van Wijk, E., Aoki, S., et al. (2018). Freshening by glacial meltwater enhances melting of ice shelves and reduces formation of Antarctic Bottom Water. *Science Advances*, *4*(4), eaap9467. https://doi.org/10.1126/sciadv.aap9467

Silvano, A., Rintoul, S. R., Peña-Molino, B., & Williams, G. D. (2017). Distribution of water masses and meltwater on the continental shelf near the Totten and Moscow University ice shelves. *Journal of Geophysical Research: Oceans*, *122*(3), 2050–2068. https://doi.org/10.1002/2016jc012115

Smedsrud, L. H., & Jenkins, A. (2004). Frazil ice formation in an ice shelf water plume. *Journal of Geophysical Research*, *109*(C3). https://doi.org/10.1029/2003jc001851

Smethie, W. M., Jr., & Jacobs, S. (2005). Circulation and melting under the Ross Ice Shelf: Estimates from evolving CFC, salinity and temperature fields in the Ross Sea. *Deep Sea Research Part I: Oceanographic Research Papers*, *52*(6), 959–978. https://doi.org/10.1016/j.dsr.2004.11.016

Smith, B., Fricker, H. A., Gardner, A. S., Medley, B., Nilsson, J., Paolo, F. S., et al. (2020). Pervasive ice sheet mass loss reflects competing ocean and atmosphere processes. *Science*, *368*(6496), 1239–1242. https://doi.org/10.1126/science.aaz5845

Spence, P., Griffies, S. M., England, M. H., Hogg, A. M., Saenko, O. A., & Jourdain, N. C. (2014). Rapid subsurface warming and circulation changes of Antarctic coastal waters by poleward shifting winds. *Geophysical Research Letters*, *41*(13), 4601–4610. https://doi.org/10.1002/2014gl060613

Stearns, L. A., Smith, B. E., & Hamilton, G. S. (2008). Increased flow speed on a large East Antarctic outlet glacier caused by subglacial floods. *Nature Geoscience*, *1*(12), 827–831. https://doi.org/10.1038/ngeo356

Stevens, C., Hulbe, C., Brewer, M., Stewart, C., Robinson, N., Ohneiser, C., & Jendersie, S. (2020). Ocean mixing and heat transport processes observed under the Ross Ice Shelf control its basal melting. *Proceedings of the National Academy of Sciences*, *117*(29), 16799–16804. https://doi.org/10.1073/pnas.1910760117

Stewart, A. L., & Thompson, A. F. (2015). Eddy-mediated transport of warm Circumpolar Deep Water across the Antarctic shelf break. *Geophysical Research Letters*, *42*(2), 432–440. https://doi.org/10.1002/2014gl062281

Stewart, C. L., Christoffersen, P., Nicholls, K. W., Williams, M. J., & Dowdeswell, J. A. (2019). Basal melting of Ross Ice Shelf from solar heat absorption in an ice-front polynya. *Nature Geoscience*, *12*(6), 435–440. https://doi.org/10.1038/s41561-019-0356-0

Thompson, A. F., Stewart, A. L., Spence, P., & Heywood, K. J. (2018). The Antarctic slope current in a changing climate. *Reviews of Geophysics*, *56*(4), 741–770. https://doi.org/10.1029/2018rg000624

Tinto, K., Padman, L., Siddoway, C., Springer, S., Fricker, H., Das, I., et al. (2019). Ross Ice Shelf response to climate driven by the tectonic imprint on seafloor bathymetry. *Nature Geoscience*, *12*(6), 441–449. https://doi.org/10.1038/s41561-019-0370-2

Tomczak, M., Jr. (1981). A multi-parameter extension of temperature/salinity diagram techniques for the analysis of non-isopycnal mixing. *Progress in Oceanography*, *10*(3), 147–171. https://doi.org/10.1016/0079-6611(81)90010-0

Wåhlin, A., Alley, K. E., Begeman, C., Hegrenæs, Ø., Yuan, X., & Graham, A. G. (2024). Swirls and scoops: Ice base melt revealed by multibeam imagery of an Antarctic ice shelf. *Science Advances*, *10*(31), eadn9188.

Wåhlin, A., Yuan, X., Björk, G., & Nohr, C. (2010). Inflow of warm Circumpolar Deep Water in the Central Amundsen Shelf. *Journal of Physical Oceanography*, *40*(6), 1427–1434. https://doi.org/10.1175/2010JPO4431.1

Wang, C., Zhang, Z., Zhong, Y., & Zhou, M. (2024). A model study of buoyancy driven cross-Isobath transport over the Ross Sea continental shelf break. *Journal of Geophysical Research: Oceans*, *129*(1), e2023JC020078. https://doi.org/10.1029/2023jc020078

Wang, Q., Danilov, S., Hellmer, H., Sidorenko, D., Schroeter, J., & Jung, T. (2013). Enhanced cross-shelf exchange by tides in the western Ross Sea. *Geophysical Research Letters*, *40*(21), 5735–5739. https://doi.org/10.1002/2013gl058207

Wang, Y., Zhou, M., Zhang, Z., & Dinniman, M. S. (2023). Seasonal variations in Circumpolar Deep Water intrusions into the Ross Sea continental shelf. *Frontiers in Marine Science*, *10*, 1020791. https://doi.org/10.3389/fmars.2023.1020791

Washam, P., Lawrence, J. D., Stevens, C. L., Hulbe, C. L., Horgan, H. J., Robinson, N. J., et al. (2023). Direct observations of melting, freezing, and ocean circulation in an ice shelf basal crevasse. *Science Advances*, *9*(43), eadi7638. https://doi.org/10.1126/sciadv.adi7638

Whiteford, A., Horgan, H., Leong, W., & Forbes, M. (2022). Melting and refreezing in an ice shelf basal channel at the grounding line of the Kamb Ice Stream, West Antarctica. *Journal of Geophysical Research: Earth Surface*, *127*(11), e2021JF006532. https://doi.org/10.1029/2021jf006532

Xie, C., Zhang, Z., Chen, Y., Wang, C., & Zhou, M. (2024). The response of Ross Sea shelf water properties to enhanced Amundsen Sea ice shelf melting. *Journal of Geophysical Research: Oceans*, *129*(7), e2024JC020919. https://doi.org/10.1029/2024jc020919

Yan, L., Wang, Z., Liu, C., Wu, Y., Qin, Q., Sun, C., et al. (2023). The salinity budget of the Ross Sea continental shelf, Antarctica. *Journal of Geophysical Research: Oceans*, *128*(3), e2022JC018979. https://doi.org/10.1029/2022jc018979

Yuan, X. (2004). ENSO-Related impacts on Antarctic sea ice: A synthesis of phenomenon and mechanisms. *Antarctic Science*, *16*(4), 415–425. https://doi.org/10.1017/s0954102004002238

Zhang, J., Zhang, X., King, M. A., & Lyu, K. (2024). A model-based investigation of the recent rebound of shelf water salinity in the Ross Sea. *Geophysical Research Letters*, *51*(18), e2023GL106697. https://doi.org/10.1029/2023gl106697